Canadian Journal of Physics
Revue canadienne de physique

Numerical simulation of MHD flow of micropolar fluid inside a porous inclined cavity with uniform/non-uniform heated bottom wall

SCHOLARONE™
Manuscripts

Numerical simulation of MHD flow of micropolar fluid inside a porous inclined cavity with uniform/non-uniform heated bottom wall

Mubbashar Nazeer[1], N. Ali, Tariq Javed

Department of Mathematics and Statistics, International Islamic University

Islamabad 44000, Pakistan

Abstract

Buoyancy driven, incompressible, and two-dimensional flow of a micropolar fluid inside an inclined porous cavity in the presence of magnetic field is investigated. The non-linear partial differential equations are solved by employing a robust Galerkin finite element scheme. The pressure term in this scheme is eliminated by using Penalty method. The results are exhibited in the form of streamlines, isotherms, local and average Nusselt numbers for two cases, namely constant and sinusoidal heated lower wall of the conduit. In both cases, the side walls of cavity are cold and upper side is insulated. The main difference between the two cases are observed from temperature contours. For constant heated bottom wall a finite discontinuity appear in temperature distribution at the corners of the bottom wall. In contrast, no such discontinuity appears in the temperature distribution for non-uniform heated bottom wall. The quantitative changes in temperature contours in different portions of cavity are identified by comparing the results for both cases. The code is also validated and benchmarked with the previous numerical data available in the literature. It is found that the magnetic field inclined at a certain angle either suppresses or enhances the intensity of primary circulations depending on the inclination of cavity. Further the average Nusselt number at the bottom wall is higher when magnetic field is applied vertically inspective of the inclination of cavity. The analysis presented here has potential application in solar collectors and porous heat exchangers.

Keywords: Buoyancy driven flow, Micropolar fluids, magnetic field, Numerical simulations, inclined porous cavity, finite element scheme.

1.1 Introduction

---

[1] Corresponding author email: mubbashariiui@gmail.com

Buoyancy driven flows inside closed cavities are of much interest to engineers, scientists and researchers due to their various applications in the field of engineering such as, well-ventilated

apartments, refreshing all types of electronic devices (computers, camcorders, VCRs, CD and DVD players, televisions, radios, videos camera etc.), accumulation of sun power, insulation of atomic power plant, etc. Beside their applications, such flows are also considered as classical problems for assessment of numerical methods and validation of Navier-Stokes codes. Several authors have studied natural convection flows in closed enclosures. A brief review of specialized literature on cavity flows is presented below.

An analytical study of natural convection flow inside a horizontal conduit is investigated by Bejan and Tien [1]. Davis [2] employed a different numerical scheme to analyze a free convection flow inside a square conduit and benchmarked the results with the previous data. Guo and Wu [3] provided a mathematical model to examine two-dimensional mixed convection transient flow and temperature stratification phenomena inside a cavity. A numerical and theoretical study of time-dependent buoyancy driven flow inside a left heated rectangular conduit was studied by Hall et al. [4]. Patterson and Armfield [5] provided a comparison between numerical and experimental study of time-dependent free convection flow inside a square conduit. Kuyper et al. [6] employed a numerical technique to simulate the natural convection flow inside a differentially hated tilted square enclosure. A steady state natural convection laminar flow in the presence of high Rayleigh number was analyzed by Ravi et al. [7]. Barakos et al. [8] employed a finite volume method for benchmarking the results of free convection flow inside a conduit. Ozoe and Maruo [9] obtained a correlation of heat transfer rate dependent on Prandtl, Rayleigh and Hartmann numbers for the buoyancy driven flow inside a square conduit. Ozoe and Okada [10] presented a mathematical model of three dimensional natural convection flow inside a cavity and examined the influence of direction of magnetic field. A numerical and analytical study of natural convection flow inside a tilted cavity in the presence of transverse magnetic field was carried out by Vasseur et al. [11]. They also benchmarked their results against the results provided by Cormack et al. [12]. Alchaar et al. [13] employed a finite difference method to investigate the natural convection flow inside a rectangular conduit in the presence of transverse magnetic and compared their solution with the previous available analytical solution accomplished by

Garandet et al. [14]. Rudraiah et al. [15] predicted the influence of transverse magnetic field on time-dependent natural convection flow inside a rectangular conduit with the help of finite difference method. The conduit side walls were maintained at a constant temperature while horizontal boundaries were insulated. The study carried out by Oreper and Szekely [16] reveals that convection currents are suppressed by magnetic field and crystal formation is linked with strength of magnetic field. Alchaar et al. [17] employed a numerical scheme to predict the influence of inclined magnetic field on buoyancy driven flow inside a rectangular conduit. Their numerical simulations demonstrated that the influence of magnetic field is to reduce the heat transfer and inhibit the beginning of convection current.

Free convection flows through porous medium have attracted much attention of researchers due to their several technical usages in geothermal reservoirs, separation processes in chemical engineering, oil exploration and solidification of castings. Vafai [18] summarized latest developments on various aspects of flow and heat transfer through porous media. The applications of fluid flow and heat transfer through porous medium in biological systems were also presented by Vafai [19]. Tong and Subramanian [20] obtained boundary layer solution based on modified Oseen technique for buoyancy driven flow inside a porous rectangular enclosure. Effects of different aspect ratio on the free convection flow inside left sided heated rectangular porous cavity were analyzed by Prasad and Kulacki [21]. Basak et al. [22] employed a finite element scheme to investigate the effects of constant and variable heated boundary on free convection flow inside a porous cavity. Walker and Homsy [23] employed different methods to investigate the buoyancy driven flow inside a differentially heated porous conduit. A numerical study for different parametric ranges of Darcy and Rayleigh number was presented by Lauriat and Prasad [24]. Basak et al. [25] employed a finite element scheme to predict the effects of various heating wall and inclination angles on free convection flow inside a trapezoidal porous enclosure. Javed et al. [26] employed a Galerkin finite element method to investigate the effects of uniform and non-uniform heated inclined walls on free convection flow inside a porous triangular conduit in presence of magnetic field.

Micropolar fluid dynamics is a branch of fluid mechanics which is concerned with motion of fluids whose material points possess orientation [27-28]. Micropolar fluid is a fluid which is concerned with rotation of fluid particles at microscale. These type of fluids are also known

as polar fluids. Liquid crystals, animal blood and polymeric suspension are some examples of micropolar fluid [27-28]. In fact, flows with rigid and randomly oriented or spherical particles embedded in a viscous medium are well described by micropolar fluid. Only rotational motion of these element is considered whereas deformation of these suspended particles is ignored in the micropolar theory. The balance law of mass and linear momentum are supplemented with principle of angular momentum to accurately describe the geometry and intrinsic motion of microelements. This results in a non-symmetric stress tensor. Due to its simplicity, the micropolar model is widely used to analyze the flows polymeric fluids with additives, blood, suspensions etc. The rigorous mathematical theory of micropolar fluids was developed by Eringen [29-31]. It is important to point out that micropolar fluid dynamics emphasizes that non-Newtonian behavior of fluid is due to intrinsic motion of the microelements and it requires the use of additional balance laws to model the flows of non-Newtonian fluids. In contrast, there is a second approach which is based techniques of microscopic non-Newtonian fluid mechanics (i.e. kinetic theory) and presents a variety of constitutive equations to capture the non-Newtonian effects. Out of these, Maxwell and Jeffrey are common non-Newtonian constitutive equations. Some recently studies regarding use of these equations to describe the flows of non-Newtonian fluids are carried out by Hayat et al. [32-34], Farooq et al. [35] and Khan et al. [36-39]. The micropolar fluid theory has also become very popular in the field of engineering and technology and several researchers used it to model isothermal hydrodynamic fluid phenomena inside closed conduits, parallel plates and over stretching rigid surfaces having industrial and engineering applications. In the next paragraph, a brief review of these attempts in presented.

Hayat et al. [40] employed homotopic approach to define the Brownian motion and thermophoresis aspect in the flow of micropolar fluid on a stretching surface. Waqas et al. [41] calculated the skin coefficients and heat transfer rate for MHD mixed convection flow of micropolar fluid on a stretching sheet. Iqbal et al. [42] employed a Keller box technique to predict the effects of inclination of magnetic field on the flow of micropolar Casson fluid over a stretching sheet. Skin friction coefficient and heat transfer rate for MHD flow of micropolar fluid between the parallel plates was analyzed by Nadeem et al. [43-44]. Tabassum et al. [45] employed the temperature-dependent viscosity model to examine the stagnation point flow of micropolar nano-fluid. Jena and Bhattacharyya [46] used the

4

Galerkin scheme based on shape function to predict the influence of microstructure on the thermal convection inside a cubical container. Chen and Hsu [47] investigated the free convection flow of micropolar fluid inside a container with aspect ratios 1, 2 and 4. A free convection flow of micropolar fluid inside an inclined conduit was studied by Wang and Hasu [48]. Bourantas and Loukopoulos [49] employed a numerical scheme to investigate the natural convection flow of a conducting micropolar nano-fluid inside a tilted cavity. A numerical study of convective flow of a micropolar fluid inside a trapezoidal cavity with constant heated bottom wall is presented by Gibanov et al. [50]. Zadravec et al. [51] developed an algorithm based on finite volume method to find numerical solution of free convection flow of micropolar fluid in a square enclosure. Gibanov et al. [52] used the finite difference scheme to analyze the free convection flow of micropolar fluid inside a differentially heated wavy cavity. Unsteady flow of a micropolar fluid in a wavy triangular conduit was studied by Sheremat et al. [53]. Alloui and Vasseur [54] reported the numerical and analytical solution of a micropolar fluid in a rectangular shallow cavity. Ece and Buyuk [55] examined buoyancy driven flow under the influence of transverse magnetic field inside an inclined cavity which is heated from left and cold from top. The left and lower wall were insulated. From the above cited literature it is noted that no such study is reported in the literature which deals with buoyancy driven flow of micropolar fluid in an inclined porous-saturated cavity under the influence of inclined magnetic field. It is intended to see how inclined magnetic field, porous medium, cavity inclination and rheological parameters of the fluid affect the flow and heat transfer rate. In fact for a presumed geometrical shape of the enclosure, our objective is to identify a suitable combination of controlling parameters for which heat transfer into the cavity is maximum/minimum. The important applications of micropolar fluid flowing through porous media can be found in porous rocks, foams and foamed solids, aerogels, alloys and polymer mixture etc. Further, the results of present study are also potentially applicable to flows of biological fluids in thin conduits, polymeric and colloidal suspensions, rigid crystals etc. Moreover, such study is also beneficial in design of room vantilation systems, solar collectors and electronic cooling system. The present study also complements the analysis of Ece and Buyuk [55] by taking the fluid inside the enclosure as a micropolar fluid and using a different set of boundary conditions i.e. both vertical boundaries of the conduit are cold whereas lower surface is maintained at constant or

sinusoidal temperature and top wall is insulated. Moreover, the space inside the cavity is also considered as porous. Physically, our model correspond to flow in a porous metal heat exchanger. Moreover, in absence of porous medium our problem models the flow and heat transfer in a solar collectors [56].

1.2 Mathematical formulations

Let us consider a two-dimensional flow of a micropolar fluid in the presence of inclined magnetic field inside a tilted porous cavity. The vertical walls of the conduit are cold whereas the top wall is insulated. A constant or variable temperature distribution is specified at the lower wall of the cavity. The geometry of the considered flow problem are shown in Fig.1. The cavity is inclined at angle w with the horizontal. A constant magnetic field of strength B is applied in the direction making an angle ϕ with lower wall of the conduit.
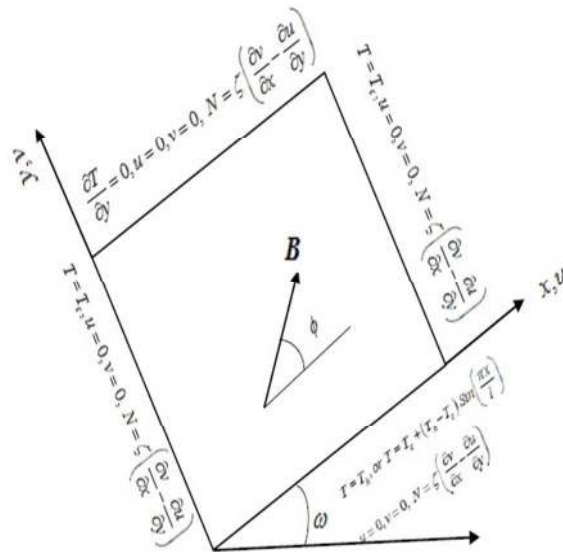

Fig. 1: schematic diagram of the consider study

The continuity, momentum, angular momentum and energy equation for flow of micropolar fluid are [29-31]:

$$\nabla.\mathbf{V} = 0, \tag{1}$$

$$\rho\frac{D\mathbf{V}}{Dt} = -\nabla p + (2\mu + \kappa)\nabla\nabla.\mathbf{V} - (\mu + \kappa)\nabla\times\nabla\times\mathbf{V} + \kappa\nabla\times\mathbf{N} + \rho\mathbf{g} + \mathbf{j}\times\mathbf{B} - \frac{\mu}{k}\mathbf{V}, \tag{2}$$

$$j\rho\frac{D\mathbf{V}}{Dt} = (\alpha + \beta + \gamma)\nabla\nabla.\mathbf{N} - \gamma\nabla\times\nabla\times\mathbf{N} - 2\kappa\mathbf{N} + \kappa\nabla\times\mathbf{V}, \tag{3}$$

6

$$\rho c_p \frac{DT}{Dt} = k\nabla^2 T,$$

(4)

In the above equations, $D(\ )/Dt = \partial(\ )/\partial t + v_k\, \partial(\ )/\partial x_k$ is the Stoke's material derivative and V, N and T denote velocity, micropolar and temperature fields, respectively. Moreover, ρ is the fluid density, c_p is the specific heat, $\bar{k}$ is the permeability of the porous medium, k is the thermal conductivity, μ is the dynamics viscosity, j is the microinertia, g is the gravitational acceleration, κ is the vortex viscosity coefficient and α, β, γ are spin gradient viscosity coefficients. The current density J has the following form

$$J = \sigma(V \times B).$$

(5)

In the above equation σ is the electrical conductivity of the fluid. It is assumed that the magnetic Reynolds number (R_m) is small and therefore the induced magnetic field due to motion of the fluid is neglected [57]. It is also assumed that the Joule heating and viscous dissipation effects are negligible.

Using the Boussinesq approximation, the governing equations in scalar form are:

$$\frac{\partial u}{\partial x} - \frac{\partial v}{\partial y} = 0,$$

(6)

$$\rho\left(u\frac{\partial u}{\partial x} + v\frac{\partial u}{\partial y}\right) = -\frac{\partial p}{\partial x} + \left(\upsilon + \frac{\kappa}{\rho}\right)\left(\frac{\partial^2 u}{\partial x^2} + \frac{\partial^2 u}{\partial y^2}\right) + \frac{\kappa}{\rho}\frac{\partial N}{\partial y} - \frac{\upsilon}{\bar{k}}u - \rho\left[1 - \beta(T - T_c)\right]g\sin\omega$$
$$+ \sigma B^2\left[v\sin\phi\cos\phi - u\sin^2\phi\right],$$

(7)

$$\rho\left(u\frac{\partial v}{\partial x} + v\frac{\partial v}{\partial y}\right) = -\frac{\partial p}{\partial y} + \left(\upsilon + \frac{\kappa}{\rho}\right)\left(\frac{\partial^2 v}{\partial x^2} + \frac{\partial^2 v}{\partial y^2}\right) - \frac{\kappa}{\rho}\frac{\partial N}{\partial x} - \frac{\upsilon}{\bar{k}}v - \rho\left[1 - \beta(T - T_c)\right]g\cos\omega$$
$$+ \sigma B^2\left[u\sin\phi\cos\phi - v\cos^2\phi\right],$$

(8)

7

$$u\frac{\partial N}{\partial x}+v\frac{\partial N}{\partial y}=-\frac{\kappa}{\rho j}\left(2N+\frac{\partial u}{\partial y}-\frac{\partial v}{\partial x}\right)+\frac{\gamma}{\rho j}\left(\frac{\partial^2 N}{\partial x^2}+\frac{\partial^2 N}{\partial y^2}\right),$$

(9)

$$u\frac{\partial T}{\partial x}+v\frac{\partial T}{\partial y}=\alpha_0\left(\frac{\partial^2 T}{\partial x^2}+\frac{\partial^2 T}{\partial y^2}\right).$$

(10)

The boundary conditions for the considered geometry are:

$$\left.\begin{array}{l} u=0,v=0, N=\zeta\left(\frac{\partial v}{\partial x}-\frac{\partial u}{\partial y}\right) \text{ at } x=0 \text{ },u=0,v=0,\ N=\zeta\left(\frac{\partial v}{\partial x}-\frac{\partial u}{\partial y}\right) \text{ at } x=l, \\[3mm] u=0,v=0, N=\zeta\left(\frac{\partial v}{\partial x}-\frac{\partial u}{\partial y}\right) \text{ at } y=0 \text{ },u=0,v=0,\ N=\zeta\left(\frac{\partial v}{\partial x}-\frac{\partial u}{\partial y}\right) \text{ at } y=h, \\[3mm] T=T_h, \qquad or \qquad T=\left(T_h-T_c\right)\sin\left(\frac{\pi x}{l}\right), \text{ at } y=0, \\[3mm] T=T_c, \text{ at } x=0 \text{ } and \text{ } x=l,\ \frac{\partial T}{\partial y}=0, \text{ at } y=h. \end{array}\right\}$$

(11)

Here T_C and T_H are the temperatures of the cold and hot boundary of the conduit, respectively, h and l are the height and length of the conduit, respectively, α_0 is the thermal diffusivity of micropolar fluid, and υ is the kinematic viscosity. The sinusoidal wall temperature at the bottom wall is selected in accord to previous available studies in the literature on the cavity flow. Specifically, Basak et al. [23], Sivasankaran et al. [58], Saeid and Yaacob [59], Natarajan et al. [60], Sarris et al. [61-62], Bouhalleb and Abbassi [63] used variable heated bottom wall with a motivation to understand the heat transfer characteristics in glass melting tank, where a number of burners placed above the glass tank give rise to periodic temperature profiles on the surface of the glass melt. The condition of sinusoidal heated bottom wall is also reported by Minkowyez [64].

Introducing the normalized quantities:

$$\hat{x} = \frac{x}{l}, \hat{y} = \frac{y}{h}, \hat{\chi} = \frac{h}{l}, \hat{u} = \frac{Hu}{\alpha_0}, \hat{v} = \frac{lv}{\alpha_0}, \hat{\theta} = \frac{T-T_c}{T_h-T_c}, \overline{N} = \frac{NL^2}{\alpha_0}, Ha = lB\sqrt{\frac{\sigma}{\mu}}, Da = \frac{\overline{k}}{l^2}$$

$$\hat{p} = \frac{\left[p + \rho g(x\sin\theta + y\cos\theta)\right]l^2}{\rho\alpha_0}, Pr = \frac{\upsilon}{\alpha_0}, Gr = \frac{g\beta_0(T_h-T_c)l^3}{\upsilon^2}, \eta = \frac{l^2}{j}, R_0 = \frac{\kappa}{\mu}$$

$$\tag{12}$$

Eqs. (6)- (10) and boundary conditions defined in (11) after dropping the bars yield:

$$\frac{\partial u}{\partial x} + \frac{\partial v}{\partial y} = 0,$$

$$\tag{13}$$

$$\frac{1}{\chi^2}\left(u\frac{\partial u}{\partial x} + v\frac{\partial u}{\partial y}\right) = -\frac{\partial p}{\partial x} + \frac{Pr}{\chi}(1+R_0)\left(\frac{\partial^2 u}{\partial x^2} + \frac{\partial^2 u}{\partial y^2}\right) + \frac{R_0 Pr}{\chi}\frac{\partial N}{\partial y} - \frac{Pr}{Da\chi^3}u - GrPr^2\theta\sin\omega$$

$$+ Ha^2 Pr\left[v\sin\phi\cos\phi - \frac{1}{\chi}u\sin^2\phi\right],$$

$$\tag{14}$$

$$u\frac{\partial v}{\partial x} + v\frac{\partial v}{\partial y} = -\frac{\partial p}{\partial y} + \chi Pr(1+R_0)\left(\frac{\partial^2 v}{\partial x^2} + \frac{1}{\chi^2}\frac{\partial^2 v}{\partial y^2}\right) - R_0\chi Pr\frac{\partial N}{\partial x} - \frac{Pr}{\chi Da}v - \chi GrPr^2\theta\cos\omega$$

$$+ Ha^2 Pr\left[u\sin\phi\cos\phi - v\cos^2\phi\right],$$

$$\tag{15}$$

$$u\frac{\partial N}{\partial x} + v\frac{\partial N}{\partial y} = -\chi Pr\eta R_0\left(2N + \frac{1}{\chi}\frac{\partial u}{\partial y} - \frac{\partial v}{\partial x}\right) + \chi Pr\left(1+\frac{R_0}{2}\right)\left(\frac{\partial^2 N}{\partial x^2} + \frac{1}{\chi^2}\frac{\partial^2 N}{\partial y^2}\right),$$

$$\tag{16}$$

$$u\frac{\partial \theta}{\partial x} + v\frac{\partial \theta}{\partial y} = \chi\frac{\partial^2 \theta}{\partial x^2} + \frac{1}{\chi}\frac{\partial^2 \theta}{\partial y^2},$$

$$\tag{17}$$

$$u = 0, v = 0, N = \zeta\left(\frac{\partial v}{\partial x} - \frac{\partial u}{\partial y}\right) \text{ at } x = 0, u = 0, v = 0, N = \zeta\left(\frac{\partial v}{\partial x} - \frac{\partial u}{\partial y}\right) \text{ at } x = 1,$$

$$u = 0, v = 0, N = \zeta\left(\frac{\partial v}{\partial x} - \frac{\partial u}{\partial y}\right) \text{ at } y = 0, u = 0, v = 0, N = \zeta\left(\frac{\partial v}{\partial x} - \frac{\partial u}{\partial y}\right) \text{ at } y = 1,$$

$$\theta = 1, \text{ or } \theta = S\sin(\pi x), \text{ at } y = 0, \theta = 0, \text{ at } x = 0 \text{ and } x = 1, \frac{\partial \theta}{\partial y} = 0, \text{ at } y = 1.$$

$$\tag{18}$$

In the above non-linear system of equations, Pr is the Prandtl number, Gr is the Grashof number, χ is the aspect ratio $\left(\chi = {}^{h}\!/\!_{l}\right)$ [42], η and R_0 are the micropolar parameters. The dimensionless parameter R_0 is the ratio of vortex viscosity parameter κ and dynamic viscosity μ. The case when vortex viscosity is zero and microelements (material fluid particles) do not possess orientation is characterized by $R_0 = 0$. In this case, the micro-rotation of material fluid particles do not affect the bulk fluid motion and as a result the fluid apparent viscosity is constant. For $R_0 > 0$, the rotational effect of material fluid particles become important. In such situation, the apparent viscosity of fluid increases with increase in deformation rate. During the derivation of above equation it is supposed that $\gamma = \left(\mu + \dfrac{k}{2}\right)j$ and $j = l^2$ [50]. The parameter of $\zeta\left(1 \geq \zeta \geq 0\right)$ is known as micro-gyration parameter. The case $\zeta = 0$ corresponds to the situation in which microelement are unable to rotate near the boundaries due to greater density of particles. The situation of weak concentration of microelements near the boundary is characterized by the case $\zeta = 0.5$. For unit value of ζ, the turbulent flow arise. We shall only present the results for the first two cases as the last case is beyond the scope of the present study.

2. Solution procedure

The partial differential equations (13)-(17) are highly non-linear. Therefore, we cannot find the exact solution of the given system. The computational solution can be find by using any numerical technique. Here we have employed a finite element scheme based on a Galerkin method [23, 26, 65, 66]. This numerical scheme presents a convenient way to gain the numerical/approximate solution of complex system of ordinary and partial differential equations. The Penalty method [65] is used to remove the pressure term in the momentum equations by using continuity equation. The penalty parameter δ is introduced by using incompressibility condition as follows:

$$p = -\delta\left(\frac{\partial u}{\partial x} + \frac{\partial v}{\partial y}\right),\tag{19}$$

The Eqs. (14), (15) will take the new form as given below

10

$$\frac{1}{\chi^2}\left(u\frac{\partial u}{\partial x}+v\frac{\partial u}{\partial y}\right)=-\frac{\partial}{\partial x}\left(\frac{\partial u}{\partial x}+\frac{\partial v}{\partial y}\right)+\frac{Pr}{\chi}\left(1+R_0\right)\left(\frac{\partial^2 u}{\partial x^2}+\frac{\partial^2 u}{\partial y^2}\right)+\frac{R_0 Pr}{\chi}\frac{\partial N}{\partial y}-\frac{Pr}{Da\chi^3}u$$

$$-GrPr^2\theta\sin\omega+Ha^2 Pr\left[v\sin\phi\cos\phi-\frac{1}{\chi}u\sin^2\phi\right],\tag{20}$$

$$u\frac{\partial v}{\partial x}+v\frac{\partial v}{\partial y}=-\frac{\partial}{\partial y}\left(\frac{\partial u}{\partial x}+\frac{\partial v}{\partial y}\right)+\chi Pr\left(1+R_0\right)\left(\frac{\partial^2 v}{\partial x^2}+\frac{1}{\chi^2}\frac{\partial^2 v}{\partial y^2}\right)-R_0\chi Pr\frac{\partial N}{\partial x}-\frac{Pr}{\chi Da}v$$

$$-\chi GrPr^2\theta\cos\omega+Ha^2 Pr\left[u\sin\phi\cos\phi-v\cos^2\phi\right],\tag{21}$$

In order to satisfy continuity equation a large value of δ taken generally equal to 10^7 returns the consistent solution.

2.2 Formulation of FEM

The finite element approximations of the velocity vector $V=[u,v,0]$, micro-rotation vector $N=[0,0,N]$ and temperature θ are of the form

$$u=\sum_{i=1}^{m}u_i\phi_i^e(x,y),\; v=\sum_{i=1}^{m}v_i\phi_i^e(x,y),\; N=\sum_{i=1}^{m}N_i\phi_i^e(x,y),\; \theta=\sum_{i=1}^{m}\theta_i\phi_i^e(x,y).\tag{22}$$

Upon using Eq. (28) into Eqs. (31) – (34), we get the residual errors of the above non-linear equations which are

$$R_j^{(1)}=\frac{1}{\chi^2}\sum_{i=1}^{m}u_i\int_{\Omega^e}\left\{\left(\sum_{i=1}^{m}u_i\phi_i^e\right)\frac{\partial\phi_i^e}{\partial x}+\left(\sum_{i=1}^{m}v_i\phi_i^e\right)\frac{\partial\phi_i^e}{\partial y}\right\}\phi_j^e d\Omega+\delta\left\{\sum_{i=1}^{m}u_i\int_{\Omega^e}\frac{\partial\phi_j^e}{\partial x}\frac{\partial\phi_i^e}{\partial x}d\Omega+\sum_{i=1}^{m}v_i\int_{\Omega^e}\frac{\partial\phi_j^e}{\partial x}\frac{\partial\phi_i^e}{\partial y}d\Omega\right\}$$

$$+\frac{Pr}{\chi}\left(1+R_0\right)\sum_{i=1}^{m}u_i\int_{\Omega^e}\left\{\frac{\partial\phi_j^e}{\partial x}\frac{\partial\phi_i^e}{\partial x}+\frac{\partial\phi_j^e}{\partial y}\frac{\partial\phi_i^e}{\partial y}\right\}d\Omega-\frac{R_0 Pr}{\chi}\sum_{i=1}^{m}N_i\int_{\Omega^e}\phi_j^e\frac{\partial\phi_i^e}{\partial y}d\Omega+\frac{Pr}{Da\chi^3}\int_{\Omega^e}\sum_{i=1}^{m}u_i\phi_i^e d\Omega$$

$$+GrPr^2\sin\omega\int_{\Omega^e}\sum_{i=1}^{m}\theta_i\phi_i^e d\Omega-Ha^2 Pr\left[\sin\phi\cos\phi\int_{\Omega^e}\sum_{i=1}^{m}v_i\phi_i^e d\Omega-\frac{1}{\chi}\sin^2\phi\int_{\Omega^e}\sum_{i=1}^{m}u_i\phi_i^e d\Omega\right]\tag{23}$$

11

$$R_j^{(2)} = \sum_{i=1}^{m} v_i \int_{\Omega^e} \left\{ \left(\sum_{i=1}^{m} u_i \phi_i^e \right) \frac{\partial \phi_i^e}{\partial x} + \left(\sum_{i=1}^{m} v_i \phi_i^e \right) \frac{\partial \phi_i^e}{\partial y} \right\} \phi_j^e d\Omega + \delta \left\{ \sum_{i=1}^{m} u_i \int_{\Omega^e} \frac{\partial \phi_j^e}{\partial y} \frac{\partial \phi_i^e}{\partial x} d\Omega \right.$$

$$+ \sum_{i=1}^{m} v_i \int_{\Omega^e} \frac{\partial \phi_j^e}{\partial y} \frac{\partial \phi_i^e}{\partial y} d\Omega \right\} + \chi Pr (1 + R_0) \sum_{i=1}^{m} v_i \int_{\Omega^e} \left\{ \frac{\partial \phi_j^e}{\partial x} \frac{\partial \phi_i^e}{\partial x} + \frac{1}{\chi^2} \frac{\partial \phi_j^e}{\partial y} \frac{\partial \phi_i^e}{\partial y} \right\} d\Omega - R_0 \chi Pr \sum_{i=1}^{m} N_i \int_{\Omega^e} \phi_j^e \frac{\partial \phi_i^e}{\partial x} d\Omega$$

$$+ \frac{Pr}{\chi Da} \int_{\Omega^e} \sum_{i=1}^{m} v_i \phi_i^e d\Omega + \chi Gr Pr^2 \cos \omega \int_{\Omega^e} \sum_{i=1}^{m} \theta_i \phi_i^e d\Omega - Ha^2 Pr \left[\sin \phi \cos \phi \int_{\Omega^e} \sum_{i=1}^{m} u_i \phi_i^e d\Omega - \cos^2 \phi \int_{\Omega^e} \sum_{i=1}^{m} v_i \phi_i^e d\Omega \right] \right\}, (24)$$

$$R_j^{(3)} = \sum_{i=1}^{m} N_i \int_{\Omega^e} \left\{ \left(\sum_{i=1}^{m} u_i \phi_i^e \right) \frac{\partial \phi_i^e}{\partial x} + \left(\sum_{i=1}^{m} v_i \phi_i^e \right) \frac{\partial \phi_i^e}{\partial y} \right\} \phi_j^e d\Omega + \chi Pr R_0 \eta \left[2 \sum_{i=1}^{m} N_i \int_{\Omega^e} \phi_j^e \phi_i^e d\Omega + \frac{1}{\chi} \sum_{i=1}^{m} u_i \int_{\Omega^e} \phi_j^e \frac{\partial \phi_i^e}{\partial y} d\Omega \right.$$

$$\left. - \sum_{i=1}^{m} v_i \int_{\Omega^e} \phi_j^e \frac{\partial \phi_i^e}{\partial x} d\Omega \right] + \chi Pr \left(1 + \frac{R}{2} \right) \sum_{i=1}^{m} N_i \int_{\Omega^e} \left\{ \frac{\partial \phi_j^e}{\partial x} \frac{\partial \phi_i^e}{\partial x} + \frac{\partial \phi_j^e}{\partial y} \frac{\partial \phi_i^e}{\partial y} \right\} d\Omega \right\}, (25)$$

$$R_j^{(4)} = \sum_{i=1}^{m} \theta_i \int_{\Omega^e} \left\{ \left(\sum_{i=1}^{m} u_i \phi_i^e \right) \frac{\partial \phi_i^e}{\partial x} + \left(\sum_{i=1}^{m} v_i \phi_i^e \right) \frac{\partial \phi_i^e}{\partial y} \right\} \phi_j^e d\Omega + \chi \sum_{i=1}^{m} \theta_i \int_{\Omega^e} \left\{ \frac{\partial \phi_j^e}{\partial x} \frac{\partial \phi_i^e}{\partial x} + \frac{1}{\chi} \frac{\partial \phi_j^e}{\partial y} \frac{\partial \phi_i^e}{\partial y} \right\} d\Omega \right\}. \quad (26)$$

The above equations (23) – (26) are the non-linear algebraic equations which are solved by using Newton's iterative scheme. The procedure we followed is given below:

2.3 Newton's iterative Scheme

Newton - Raphson method is used here to get the higher order of convergence. Let us transform the above system into Newton - Raphsan form as

$$J \left(a^b - a^{b+1} \right) - R \left(a^b \right) = 0, \quad (27)$$

where $J(a^b)$ is the jacobian matrix which consist of all derivatives of the non-linear residual system of component of the velocity u, v micro-polar rotation vector N and temperature θ, $R(a^b)$ is the vector of residual and b is the iterative index.

3. Computation of Heat transfer rate and stream function

i) Stream function and Nusselt number

The components of the velocity and stream function are calculated numerically by using the technique given in [23]. The local Nusselt numbers Nu is given by

$$Nu = -\frac{\partial \theta}{\partial n},$$

(28)

where n is the direction normal to the plane. The local Nusselt number at vertical and bottom walls have the following general expression:

$$Nu_b = -\chi \sum_{i=1}^{m} \theta_i \frac{\partial \phi_i^e}{\partial y} \quad \text{and} \quad Nu_s = -\chi \sum_{i=1}^{m} \theta_i \frac{\partial \phi_i^e}{\partial x}$$

(29)

Averaging over the length of bottom and vertical walls, we get

$$\overline{Nu_b} = \chi \int_0^1 Nu_b dx \quad \text{and} \quad \overline{Nu_s} = \chi \int_0^1 Nu_s dx,$$

(30)

as average Nusselt numbers.

Table 1

Average Nusselt number at the lower wall of the conduit for the case of sinusoidal heated wall

No. of six nodal triangular elements	χ	ω	Gr	ϕ	Da	Ha	ξ	R_0	η	$\overline{Nu_h}/\chi$	% Error
1024	1	45^0	10^5	45^0	10^{-3}	100	0.5	2	1	2.1365	----
2048	----	----	----	----	----	----	----	----	----	2.1320	0.21
3072	----	----	----	----	----	----	----	----	----	2.1303	0.08
4096	----	----	----	----	----	----	----	----	----	2.1300	0.01

4. Algorithm validation

To ensure the optimal solution of the given problem, the grid independent test is very important. Various mesh sizes are used to perform the numerical simulations of the considered problem and it is noted that, when the computational mesh containing 4096 triangular elements is refined to 4096 elements, the percentage error between the computed results obtained at two mesh sizes is 0.01% (Table 1). A further mesh refinement can be made to reduce the error but at very high computational cost. Moreover, refining the mesh with increasing the nodal elements from 4096

do not significantly alter the physical features. Therefore, we have used the non-uniform mesh of 4096 triangular elements to investigate the present problem. After achieving grid independence, the developed code is validated against the results of Ece and Buyuk [55]. To this end, we have solved the Eqs. 11-14 of paper by Ece and Buyuk [55] using our own developed code. The results for stream function and temperature for $Pr = 1, \chi = 1, Ha = 50, Gr = 10^4, \phi = \omega = 45^0$ are shown in Fig. 2 in the form of contours. In Fig.2, the dotted line contours are plotted from our numerical solutions. The superimposed asterisks in each contours represent the values of stream function and temperature based on the solution computed by Ece and Buyuk [55]. Figure 2 shows an excellent agreement between numerical results based on our code with the corresponding results of Ece and Buyuk [55]. This obviously corroborates the validity of our numerical code and thus the confidence on results produced in the next section is quite high.

5. Numerical results

Numerical simulations of the problem under investigation are carried out for different values of Prandtl number valid for liquid metals, air, water, glycerol and polymer melts. The angle of inclination ω of the conduit is selected in the range $-45^0 \leq \omega \leq 45^0$. The aspect ratio for the square conduit is equal to unity. The flow equations evidently show that the magnitude of Ha and Gr are playing an important role to build a buoyancy or magnetic force dominant flow field inside the cavity. It is known that the buoyancy forces are logically much active for greater values of Grashof number. Whereas Lorentz force impedes the flow and retains the convection currents. The specific ranges of various parameters involved in the simulations are: $0 \leq Ha \leq 150, 10^{-5} \leq Da \leq 10^{-2}, 0 \leq R_0 \leq 12$ and $0^0 \leq \phi \leq 90^0$. The other micropolar parameter η is fixed at a unit value.

5.1 Uniform heated bottom wall

In the present section, the numerical results are reported for the first case namely, uniform heated lower wall of the cavity. Figs. 3-7 exhibit the effects of pertinent physical parameters on the streamlines and isotherms. The effects of ω (angle of inclination of cavity) and ϕ (angle of inclination of magnetic field) on streamlines and isotherms are displayed in Figs. 3 and 4, respectively. For the case when magnetic field is parallel to x-axis ($\phi = 0^0$) and $\omega = 45^0$,

14

the cavity is filled with both clockwise and anticlockwise circulations. The strength and size of clockwise circulations is greater than the strength of anticlockwise circulations. The strength of counter clockwise circulations increases with increasing ϕ to 45^0 or 90^0. With increasing ϕ to 45^0 or 90^0 the anti-clockwise circulating roll also increases in size. It is noted that for $\omega = 45^0$ there does not exist any value of ϕ for which the circulations are symmetric about the vertical centerline. In contrast, for $\omega = 0^0$, the circulating rolls become symmetric for $\phi = 0^0$ and $\phi = 90^0$. Similarly, no symmetric pattern of streamlines is noted for any value of ϕ when $\omega = 45^0$. In that case an increase in ϕ results in the formation of strong clockwise circulating roll in the right half of the cavity. Fig. 4 reveals that for each fixed value of ω and $\phi = 0^0$, the contours of different values of θ spanning the entire cavity rise toward the top adiabatic wall. However, with increasing ϕ, these contours are suppressed toward the bottom wall.

Fig. 5 illustrates the effects of Prandtl number on streamlines and isotherms in a cavity inclined at 45^0 for the case $Gr = 10^6$. The objective is to see the isotherms and streamlines for very low, moderate and large values of Prandtl number. The values $Pr = 0.015$ and 7 are typical for liquid mercury and water while the values $Pr = 10^3$ and $Pr = 10^4$ correspond to glycerol and polymer melts, respectively. It is observed that for $Pr = 0.015$ (for high thermal conductivity fluids) the counterclockwise circulations which are composed of two circulating rolls occupy the major portion of the cavity. The distorted clockwise circulations exist only in right half of the cavity. All these circulating rolls constitute an asymmetric pattern of streamlines inside the cavity. The intensity of circulations is low and heat transfer is mainly due to conduction and that is why the corresponding isotherms are less distorted. With increasing Prandtl number to 10^3 both the strength and size of counterclockwise circulations increase. The convection effect becomes prominent and isotherms lose their symmetry. Due to stronger counterclockwise circulations, the isotherms are pushed toward the right wall. Moreover, the contour for $\theta = 0.4$ split into two contour lines. For $Pr = 10^4$ both strength and size of anti-clockwise circulations increase while clockwise circulations diminish and can only be found in lower right corner of the cavity. The corresponding isotherms are pushed toward the right wall. Moreover, in this case the two contour lines for $\theta = 0.4$ reunite into a single contour.

The streamlines and isotherms for different values of Darcy number in a cavity tilted at 45^0 are shown Fig. 6. For this case, the streamlines are composed of two asymmetric rotating rolls in

15

absence of porous medium $(Da \to \infty)$. The size of anticlockwise rotating roll is much bigger than the clock rotating roll. With increasing Darcy number (decreasing the permeability of the porous medium), the anticlockwise roll increases in size and occupies the entire cavity. In fact, a decrease in permeability of the medium impedes the flow and retains the convection currents. Moreover, the strength of circulation is greatly reduced with decreasing Darcy number. The isotherms for $Da = 10^{-3}$ which are distorted and asymmetric about the vertical centerline become symmetric when Da takes the value 10^{-5}.

The effects of micropolar parameter or vortex viscosity parameter R_0 on streamlines and isotherms are presented through Fig. 7. The parameter R_0 in the present problem is a measure of increase in the apparent viscosity of the fluid. Larger values of R_0 correspond to fluids with greater apparent viscosity and vice-versa. Here, it is noted that an increase in R_0 impedes the strength of both clockwise and anticlockwise circulations. This is due to increase in the effective/apparent viscosity of the fluid due to strong rotation of the fluid particles. For larger values of R_0 the cavity in filled with weak intensity anticlockwise circulations except in the top right corner where a small weak clockwise circulating roll can be identified. The isotherms indicate the suppression of temperature contour with increasing R_0. The isotherms plot for $R_0 = 12$ clearly portray the conduction dominant heat transfer mode in the cavity.

5.2 Non-uniform heated bottom wall

The streamlines and isotherms for the case of non-uniform heated bottom wall are shown through Fig. 8 - 12. Figs. 8 and 9 report the effects of ω and ϕ on streamlines and isotherms, respectively for same values of the involved parameters as used in Fig. 3 and 4. Similar trends are noted for non-uniform heating case as observed for uniform heating case by comparing Figs. 5 and 10 except some minor details. For instance, in contrast to uniform heating case the non-uniform heating case for $Pr = 0.015$ only confirms the existence of two asymmetric circulating rolls. Moreover, for $Pr = 10^3$ the two contour lines for $\theta = 0.4$ in uniform heating case reunite into single contour for non-uniform heating case. A comparison of Figs. 3 and 8 reveals that for non-uniform heating case the anticlockwise circulating rolls for $\omega = -45^0$ and $\phi = 0^0, 45^0, 90^0$ are bigger than their counterparts for uniform heating case. No significant changes are observed between results of both cases for $\omega = 0^0$ and $\phi = 0^0, 45^0, 90^0$ except larger circulating intensity in uniform heating case. For the case when $\omega = 0^0$ and $\phi = 0^0, 45^0, 90^0$ the clockwise

circulating roll appearing in the cavity for non-uniform heating case is bigger in size than for uniform heating case. A comparison of Figs. 4 and 9 shows the contour for $\theta = 0.5 - 0.9$ spanning the entire cavity for non-uniform heating case are more suppressed in comparison to their counterpart for uniform heating case. Moreover, contrary to the uniform case the two contour lines for $\theta = 0.5$ for $\omega = 0^0, \phi = 0^0, 45^0, 90^0$ reunite into single contour spanning the entire cavity for non-uniform heating case. One obvious thing noted by comparing Figs. 4 and 9 is the disappearance of singularity from the left and right corners of the cavity for non-uniform heated case. By comparing Figs. 6 and 11, it is noted that in contrast to uniform heating case clockwise circulations do not disappear inside the cavity by decreasing Darcy number to 10^{-5} for non-uniform heating case. Moreover, the contour for $\theta = 0.1$ splits into two contour lines for uniform heating case. A comparison of Figs. 7 and 12 reveals that clockwise circulations decay faster in uniform heating case. Moreover, by comparing results for both figures it is found that the strength of circulations is greater in uniform heating case. The effects of micro-gyration parameter ξ on streamlines and isotherms can be observed by comparing Fig. 13 with Fig. 12. The results indicate that there is no appreciable effect of ξ on streamlines and isotherms.

5.3 Local Nusselt Number at the heated surface of the conduit

Fig. 14 (a) shows the effects of micropolar parameter R_0 on the local heat transfer rate for both considered cases namely, uniform and non-uniform/sinusoidal heated lower surface of the enclosure when $Gr = 10^6, Da = 10^{-3}, Ha = 10, \phi = \omega = 45^0$ and $\eta = 1$. The choice of parameters clearly indicates that both cavity and magnetic field are inclined at angle of 45^0. For the first case (uniform heating) the local heat transfer rate attains maximum value at the left edge of the lower surface due to jump discontinuity existing at edges of the lower wall and minimum at $x = 0.78$ due to inclined conduit with counterclockwise direction. The local Nusselt number decreases with increasing micropolar parameter in the interval $0 \leq x \leq 0.74$ and reverse trend can be observed in the regime $0.76 \leq x \leq 1$. On the other hand for the second case (sinusoidal heating), the maximum value of local heat transfer rate appears at $x = 0.35$ and minimum at right edge of the lower surface. Here, the local Nusselt number decrease with increasing micropolar parameter in the interval $0 \leq x \leq 0.62$ and reverse trend can be observed in the regime $0.62 \leq x \leq 1$. Fig. 14 (b) reveals that minima in the local Nusselt number profiles shift toward the left wall while maxima appearing at the left corner decreases with increasing Hartman number

for uniform heating case. Moreover, maxima in the local Nusselt number profiles also shift toward the right wall with increasing Hartmann number for non-uniform heating case. Fig. 14 (c) shows a decrease in the local Nusselt number with increasing the permeability of the porous medium $(Da \rightarrow \infty)$ for both uniform and non-uniform heating cases over major portion of the lower wall. The effects of inclination angle ω on the local Nusselt number are shown in Fig. 14 (d). In all profiles $\phi = 0^0$, therefore the maxima appear at both right and left edges of the bottom wall for uniform heating case. Moreover, the minima (maxima) in local heat transfer rate profiles shift toward the right wall with increasing ω for uniform heating case (non-uniform heating case). With increasing ω the local heat transfer rate increases in the left half of bottom wall while a reverse trend is noted in the right half for both uniform and non-uniform heating cases.

5.4. Average Nusselt Number at the hot wall

Numerical values of average Nusselt number at the bottom wall for various values of Gr, ω and ϕ are listed in Table 3 for both uniform and non-uniform heating cases. It is observed that average Nusselt number is independent of ω and ϕ for smaller values of Gr. For larger values of Gr, an increase in average Nusselt number is noted with increasing both ω and ϕ. Moreover, a rapid increase in average Nusselt number is achieved with increasing Grashof number for $\omega = -45^0$ or 45^0. Further, the average Nusselt number is substantially low for non-uniformly heated case in comparison to the uniformly heated case. Table 4 enlists the numerical values of average Nusselt number for different values of Da, R_0, Pr and Ha for both uniform and non-uniform heating cases when $Gr = 10^5$. It is noted that average Nusselt number decreases with increasing either of these parameter for both uniform and non-uniform hating case.

6. Discussion

The thermal boundary conditions imposed at the walls of the cavity in absence of the parameters ω, ϕ, Ha, R_0 induce the buoyancy driven flow inside the square cavity. The warm fluid from the middle portion of the cavity rise along the two cold vertical walls and form two symmetric rolls with clockwise and anticlockwise rotations in the enclosure. The temperature contours are symmetric about the vertical centerline. The scenario entirely resembles with situation investigated in a great deal by Basak et al. [66]. Now with increasing either of ω, ϕ, Ha and R_0 a substantial change in the pattern of streamlines and isotherms is anticipated. The

18

parameter ω is a measure of inclination angle of the cavity. The parameter ϕ determines the direction of applied magnetic field; $\phi = 0^0$ corresponds to magnetic field parallel to lower wall, $\phi = 45^0$ corresponds to the situation in which magnetic field is applied diagonally and similarly the situation in which magnetic field acts in direction perpendicular to the bottom wall is characterized by $\phi = 90^0$. The parameter Ha characterized the strength of the applied magnetic field. The rheological parameter R_0 is the ratio of vortex viscosity κ and dynamics viscosity μ. For $R_0 > 0$, the rotational effect of material fluid particles become significant which results in an increased apparent (shear-dependent) viscosity of the fluid. Having established the physical meanings of the involved parameter, we now turn to the discussion of the observed results. For $\omega = 0^0$ and $\phi = 0^0$ (the magnetic field applied in x-direction) vortices are symmetric about the vertical centerline. For $\omega = 45^0$ and $\phi = 0^0$ the buoyancy effects resists (assists) the flow in the right (left) half of the cavity. Due to this fact, the clockwise circulations diminish while anticlockwise circulations grow in entire part of the cavity. The situation is reversed for $\omega = -45^0$ and $\phi = 0^0$. Now magnetic field applied diagonally or vertically to any of these situations either increase or decrease the intensity of convection currents. For $\omega = -45^0$ and $\phi = 0^0$, the change in the direction of applied magnetic field slightly increases the intensity of clockwise circulations and at the same time accelerates the counterclockwise circulations. For $\omega = 45^0$ and $\phi = 0^0$, the similar setting enhances the intensity of counterclockwise circulations and at the same time induces the clockwise circulations. For $\omega = 0^0$ the application of diagonal magnetic field produces two asymmetric rolls occupying almost the equal portions of the cavity. Interestingly, for $\omega = 0^0$ the application of magnetic field in vertical direction results in the same symmetric flow pattern but with increased intensity as compared to the case $\omega = 0^0$ and $\phi = 0^0$. In fact, for $\omega = 0^0$ and $\phi = 0^0$ the Lorentz force term only appear in the y-momentum equation and hence does not affect the symmetry of the flow pattern. Similarly, the case $\omega = 0^0$ and $\phi = 90^0$ results in the contribution of Lorentz force term in x- momentum equation and therefore the resulting flow pattern is also symmetric. For other cases in which Lorentz force term appears in both x and y-momentum equations, the resulting flow pattern is asymmetric. The isotherms when both clockwise and anticlockwise rolls exist with one roll occupying the major portion of the cavity ($\omega = -45^0, 45^0, \phi = 0^0, 45^0, 90^0$), represents the conduction dominant heat transfer case. In this situation only few temperature contours occur asymmetrically near the

19

side walls. While rest of contours are smooth asymmetric curves spanning the entire cavity. It is noted that the contour for $\theta = 0.5$ show the tendency of splitting into two contour lines only for the cases $\omega = 45^0, \phi = 0^0$ and $\omega = 45^0$ and $\omega = 0^0$. Thus these two cases as compared to other four cases are convection dominant. The symmetric case arises only when the circulating rolls are symmetric $\omega = 0^0, \phi = 0^0$ or 90^0. In symmetric case the isotherms for $\theta = 0.5 - 0.1$ occure symmetrically along the side wall. The significant temperature gradients near the side and bottom walls indicate the development of thermal boundary layer. The streamlines for case $\omega = \phi = 0^0$ and $\omega = 0^0, \phi = 90^0$ look similar but isotherms are not. A comparison of both cases reveal that the case $\omega = 0^0 = \phi$ is convection dominant compare to the case $\omega = 0^0, \phi = 90^0$. In the next part of the discussion to our aim is to elaborate the effects of Prandtl number, Darcy number and micropolar parameter for typical cavity and magnetic field inclination angles i.e. $\omega = 45^0 = \phi$. For the case when both cavity and magnetic field are inclined at angle of 45^0 and when Grashof number is high and magnetic field is strong, it is natural to anticipate on the basis of our previous discussion that flow pattern will be asymmetric with the low intensity of circulations for fluid with small Prandtl number. The size of anticlockwise roll is bigger than that of clockwise roll. With increasing Prandtl number to 10^3 both intensity and size of anticlockwise circulations increase. Moreover, for this case the intensity of clockwise circulations also increases. In such scenario, the convection effects become significant and as a results the temperature contour start splitting but due to bigger anticlockwise roll are pushed toward the right wall. When Prandtl number takes the value 10^4 the size of clockwise circulating roll diminishes and cavity is mostly filled with anti-clockwise circulation. This scenario is not favorable for convective heat transfer. The temperature contours reunite instead of splitting into two contour line and at the same time pushed toward the right wall. The conduction is dominant in this case.

Another important parameter in our analysis is Darcy number. For a typical situation when both cavity and magnetic field are inclined at 45^0, Hartmann number is moderate, Grashof number is high, fluid inside the cavity is of high thermal conductivity ($Pr = 1$) and when permeability of the porous medium is low ($Da = 10^{-3}$), the flow in view of our previous discussion exhibits pattern comprising of counterclockwise roll occupying the maximum portion of the cavity. With decreasing Darcy number the clockwise circulations vanish and cavity is only filled with low intensity counterclockwise circulations. Decreasing the permeability of porous

results in greater resistance offered by the porous matrix to the flow induced by convection. The suppression of convection currents leads to symmetric temperature contours inside the cavity. In such scenario, heat transfer is mainly due to conduction. The effect of increasing micropolar parameter is similar to the decreasing Darcy number i.e. an increase in R_0 diminishes the clockwise circulations and also reduces the intensity of anticlockwise circulations. In fact, an increase in R_0 results in an increase in the effective viscosity of fluid and this leads to suppression in the strength of convection currents. Thus, the contours for various values of θ spanning the entire cavity are suppressed toward the bottom wall. The thermal boundary layer instead of developing at the side and bottom walls grows inside the entire cavity. Table 3 and 4 show that for fixed values of Prandtl number, Darcy number and micropolar parameter the average Nusselt number at the bottom wall of inclined cavity is maximum when Grashof number is high and when magnetic field is inclined at 90^0. The above result is true for both uniformly and non-uniformly heated cavity. A decrease is average Nusselt number is observed with increasing either of Darcy number, Prandtl number, Hartmann number and micropolar parameter. The results suggest three possible ways to increase the heat transfer from the bottom wall for a given fluid flowing inside the porous cavity. One remedy is to increase slightly the permeability of the porous medium, the second one is to adjust the inclination of angles of cavity and applied magnetic field and third one is to tune the rheological characteristics of the fluid.

Conclusions

Magnetohydrodynamic natural convection flow of micropolar fluid inside a porous-saturated cavity is numerically simulated using a robust finite element scheme for various values of Grashof number, Prandtl number, Hartmann number, micropolar parameter and inclination angles. The study can be summarized in the following main points:

➢ The clockwise circulations dominate inside the porous cavity tilted at 45^0 when flow is subject to magnetic field applied parallel to the bottom wall. The intensity of anticlockwise circulations increases with increasing the inclination angle of the magnetic field. The opposite trend prevails when cavity is inclined at 45^0. For $\omega = 0^0$, the flow pattern is symmetric when inclination angle of magnetic field is 0^0 or 90^0. The strength of circulating rolls in greater in later case. The corresponding isotherms reveal convection dominant heat transfer for $\omega = -45^0$

21

or 45^0 and when inclination angle of magnetic field is zero. Similar result is also true for non-inclined cavity ($\omega = 0^0$).

➢ The flow inside the cavity (for which $\phi = \omega = 45^0$) only comprises of weak anti-clockwise circulations with decreasing the permeability of porous media. The isotherms achieve symmetric patterns thereby indicating conduction dominant heat transfer.

➢ For cavity with $\phi = \omega = 45^0$, an increase in rheological of fluid (R_0) decreases the intensity and size of clockwise circulating roll. At the same time the size of anticlockwise roll increases but its intensity remains low. The isotherms spanning the entire cavity are compressed toward the bottom wall with increasing R_0.

➢ The average Nusselt number achieves maximum value for a specific fluid with presumed geometrical configuration of the cavity when (i) magnetic field is applied vertically, (ii) when the permeability of the media is high and (iii) when rheological parameter R_0 is small.

(a)   (b)
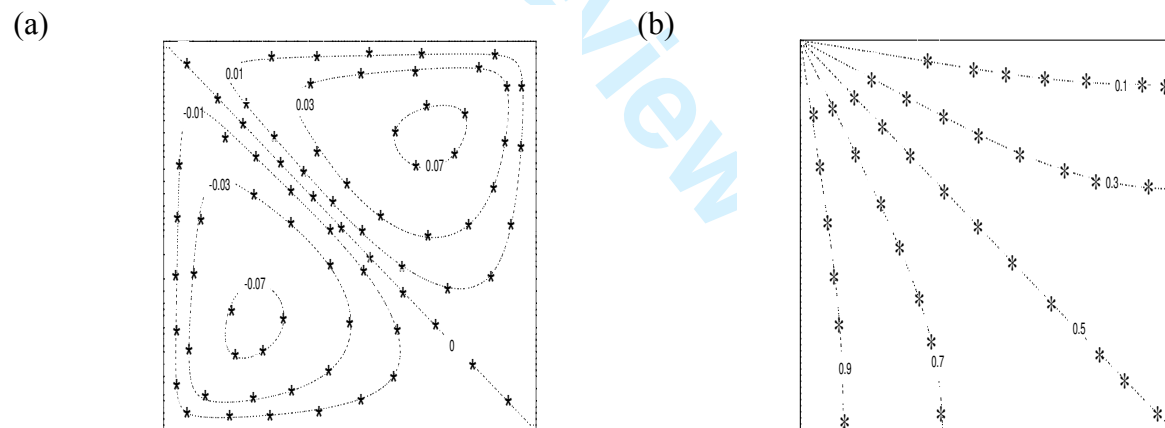
Fig 2: Streamlines (a) and temperature (b) contours for $Gr = 10^4, Ha = 50, \omega = \phi = 45^0$

$\phi = 0^0$ $\phi = 45^0$ $\phi = 90^0$

$\omega = -45^0$

$\omega = 0^0$

$\omega = 45^0$
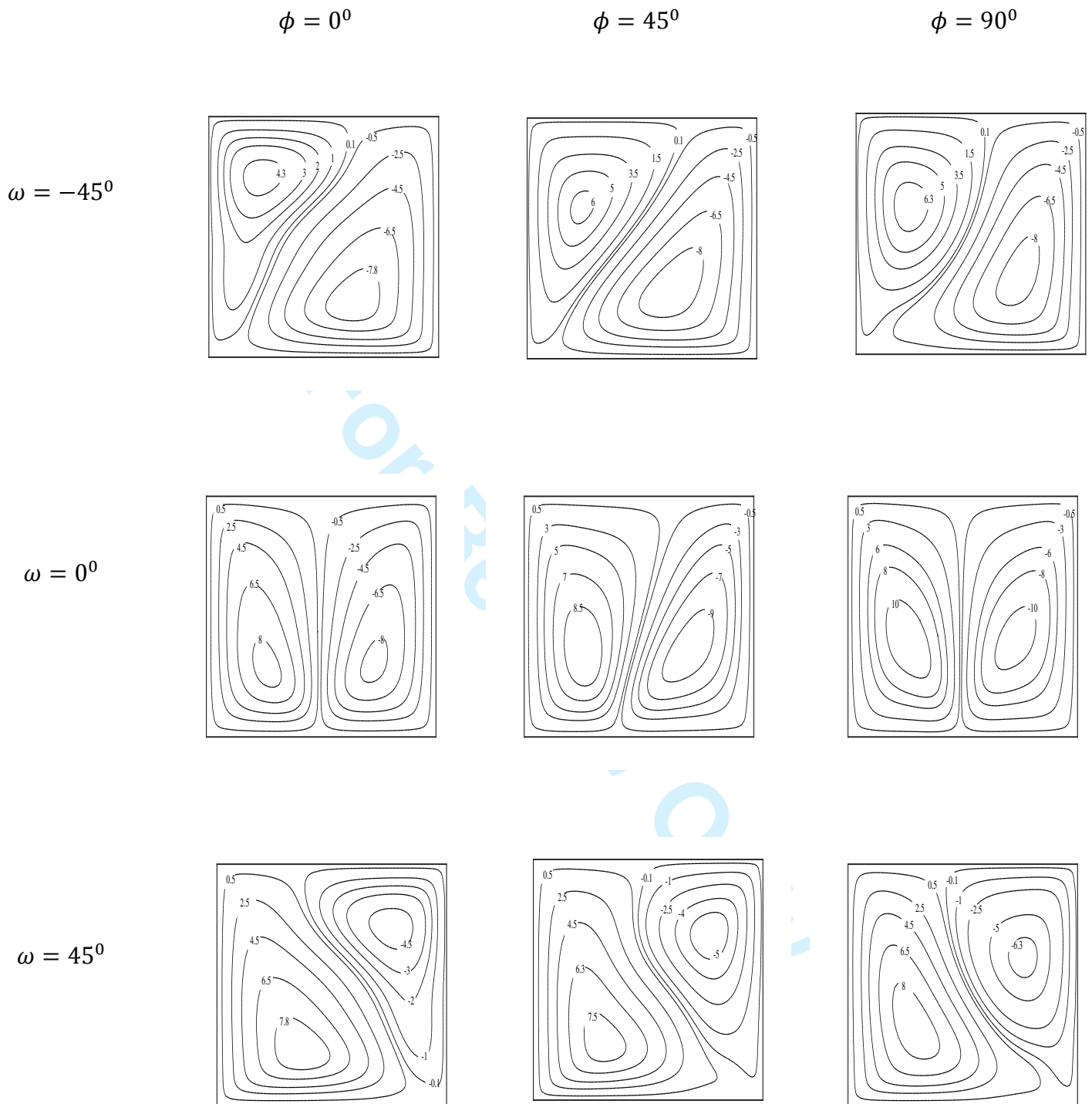
Fig 3: Effects of ϕ and ω on streamlines for $Gr = 10^6, R_0 = 2, Da \leq 10^{-3}, Ha = 50, \chi = 1$.

$\phi = 0^0$ $\phi = 45^0$ $\phi = 90^0$
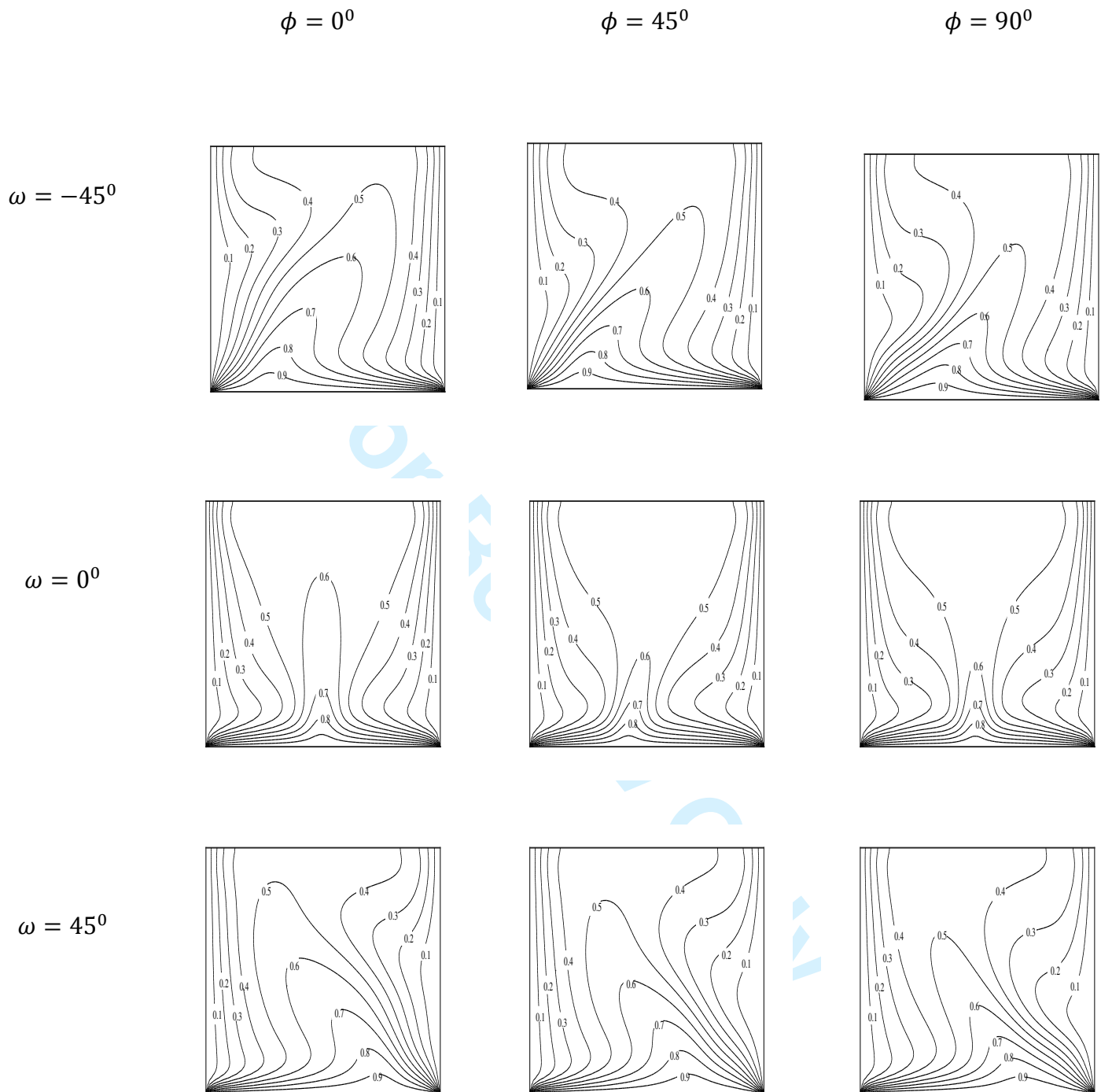
$\omega = -45^0$

$\omega = 0^0$

$\omega = 45^0$

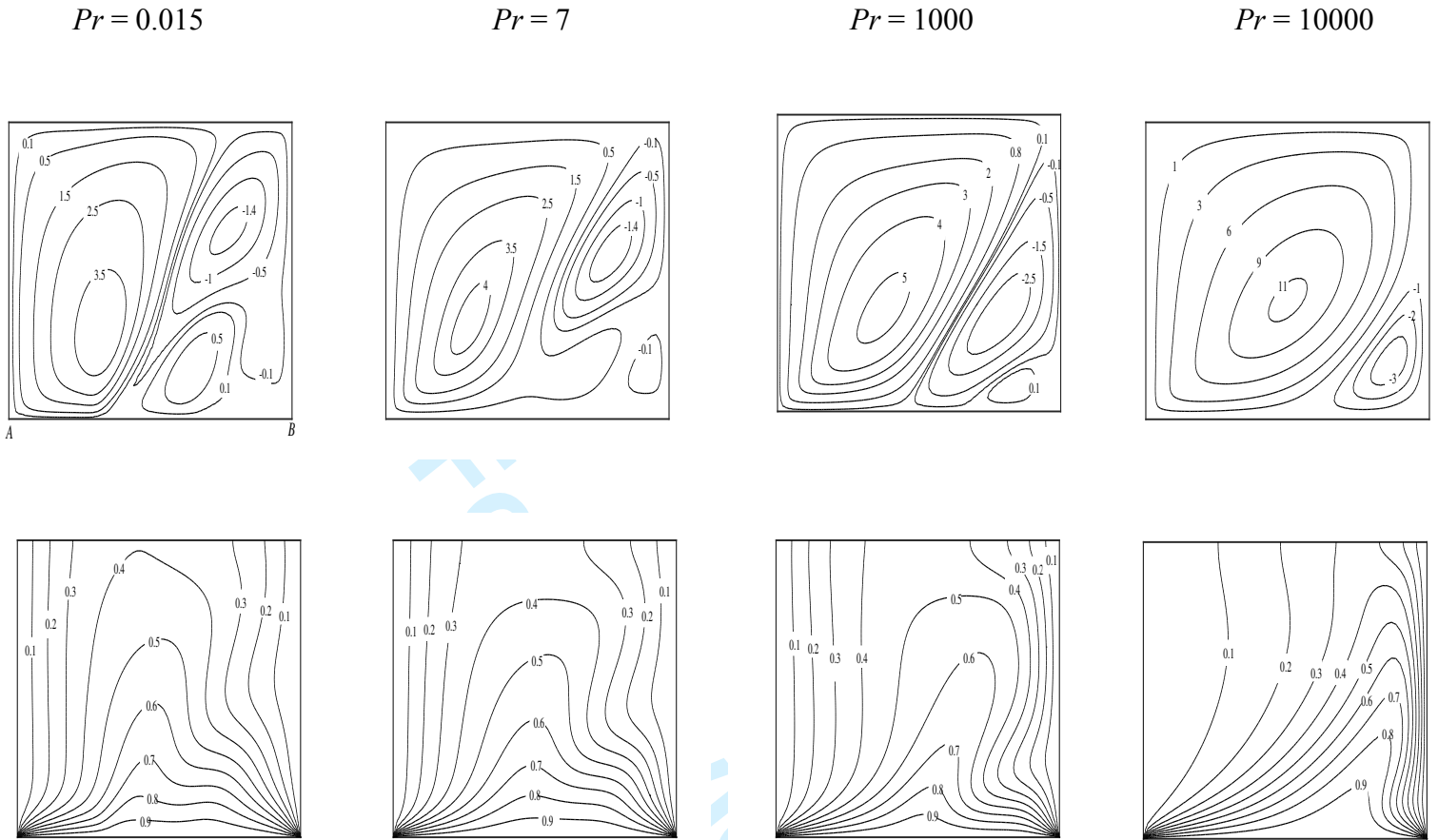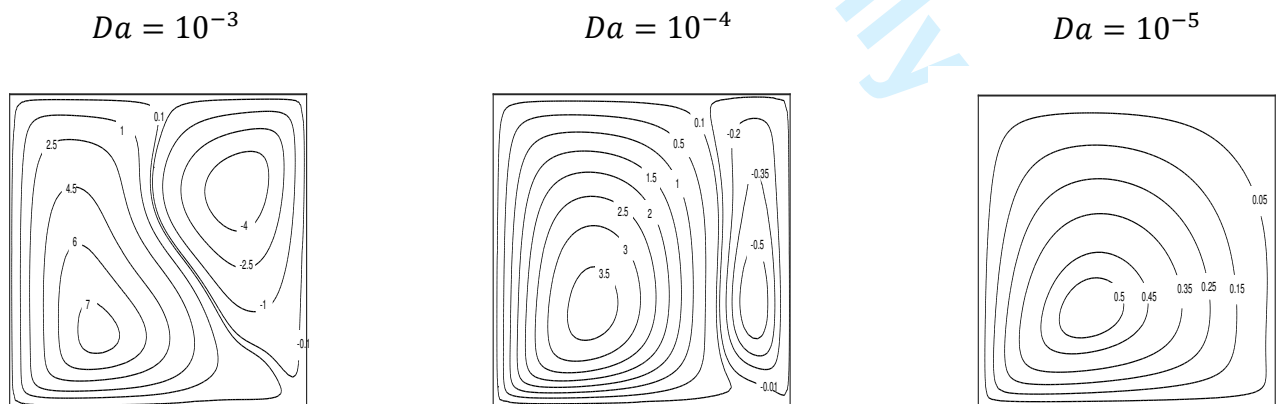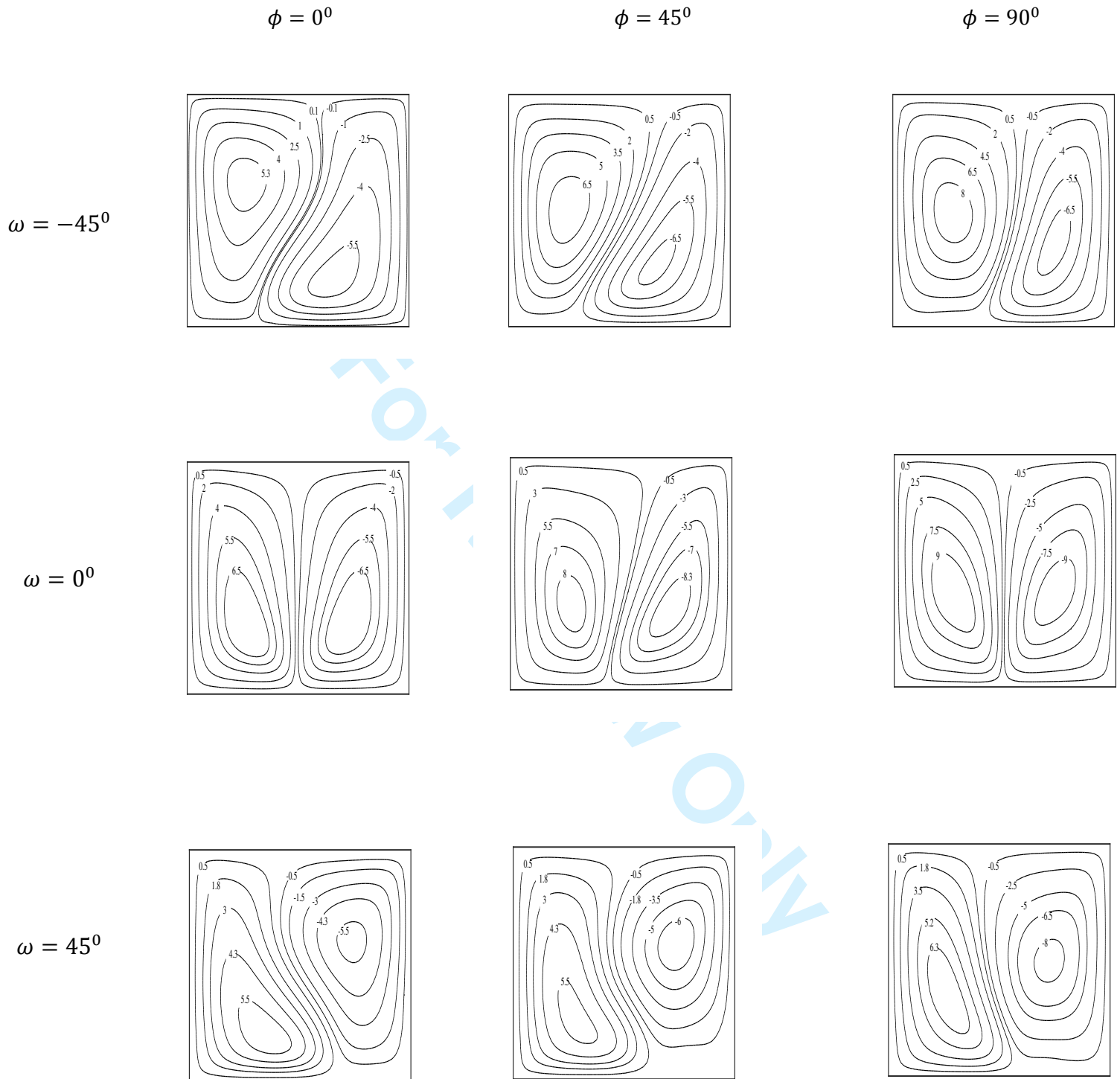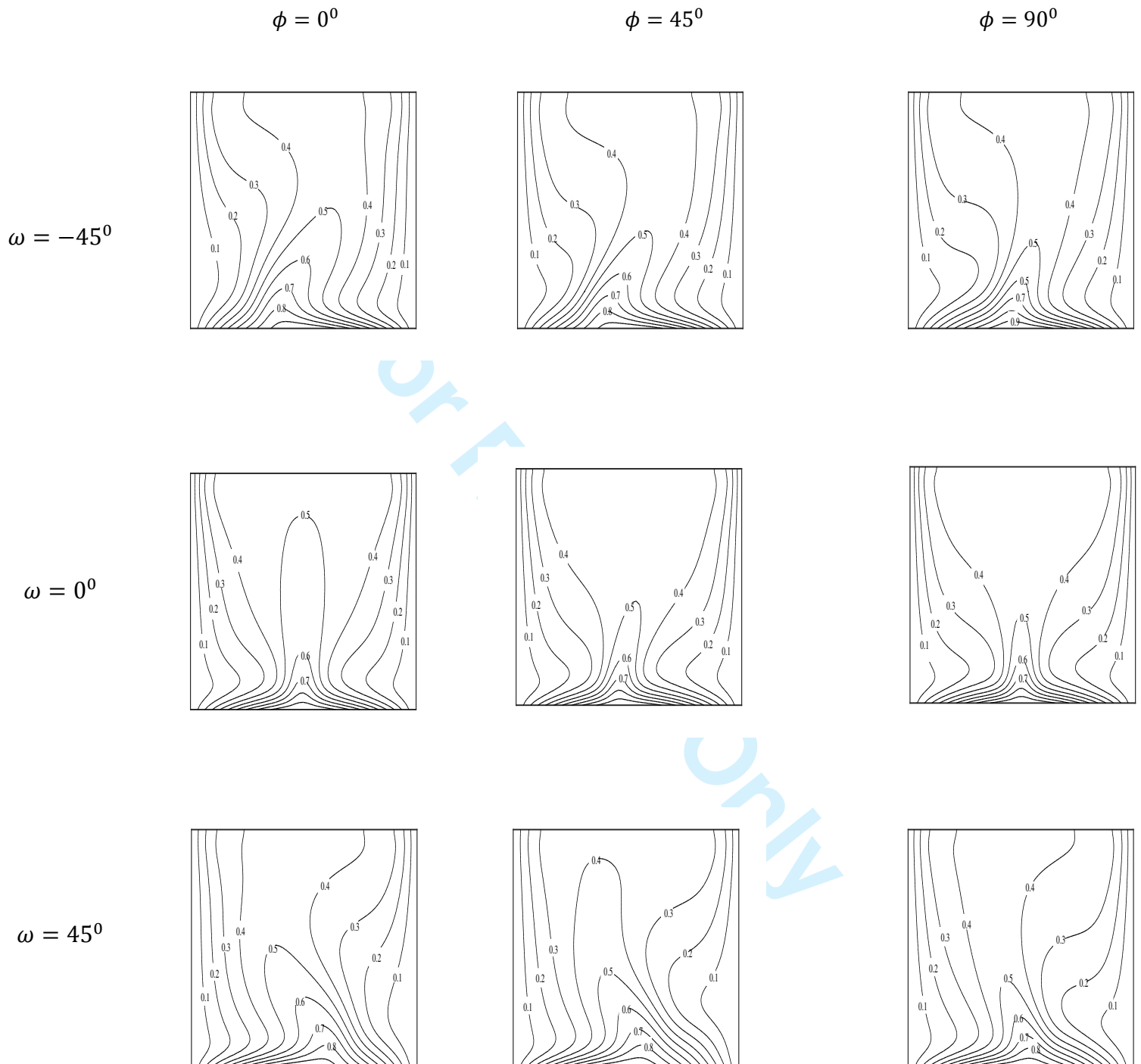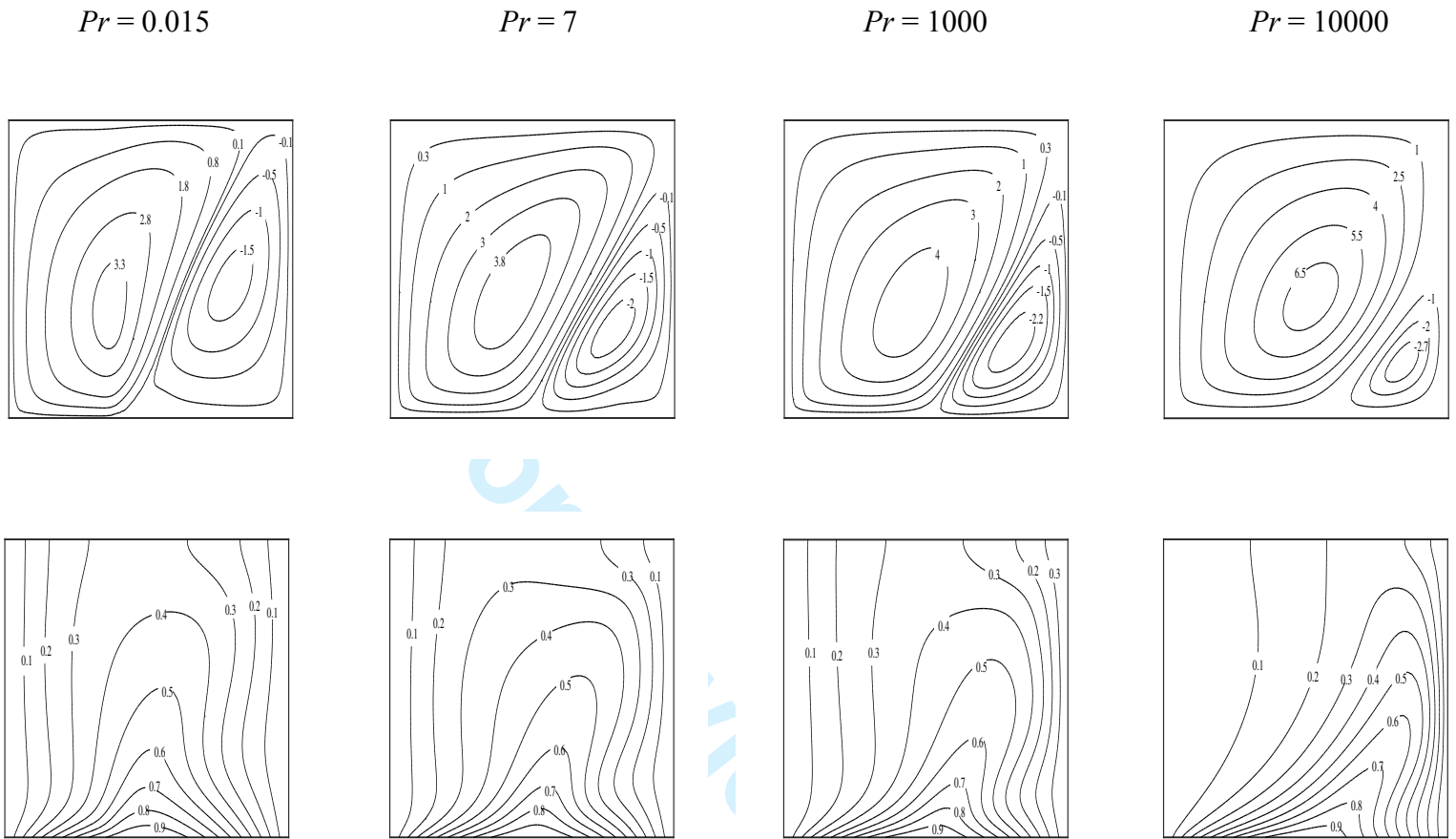Fig 4: Effects of ϕ and ω on isotherms for $Gr = 10^6, R_0 = 2, Da = 10^{-3}, Ha = 150, \chi = 1$.

Fig. 5: Effects of Prandtl number on streamlines and isotherms for $Gr = 10^6, R_0 = 2, Ha = 60, \phi = \omega = 45^0$ and $Da = 10^{-3}$.

$Da = 10^{-3}$ $Da = 10^{-4}$ $Da = 10^{-5}$

25
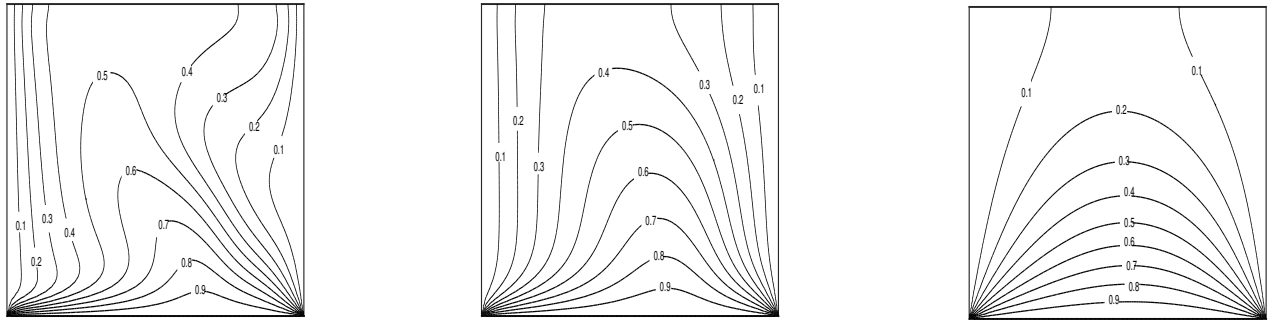
Fig. 6: Effects of Darcy number on streamlines and isotherms for $Gr = 10^6, R_0 = 2, Ha = 50, \phi = \omega = 45^0$.
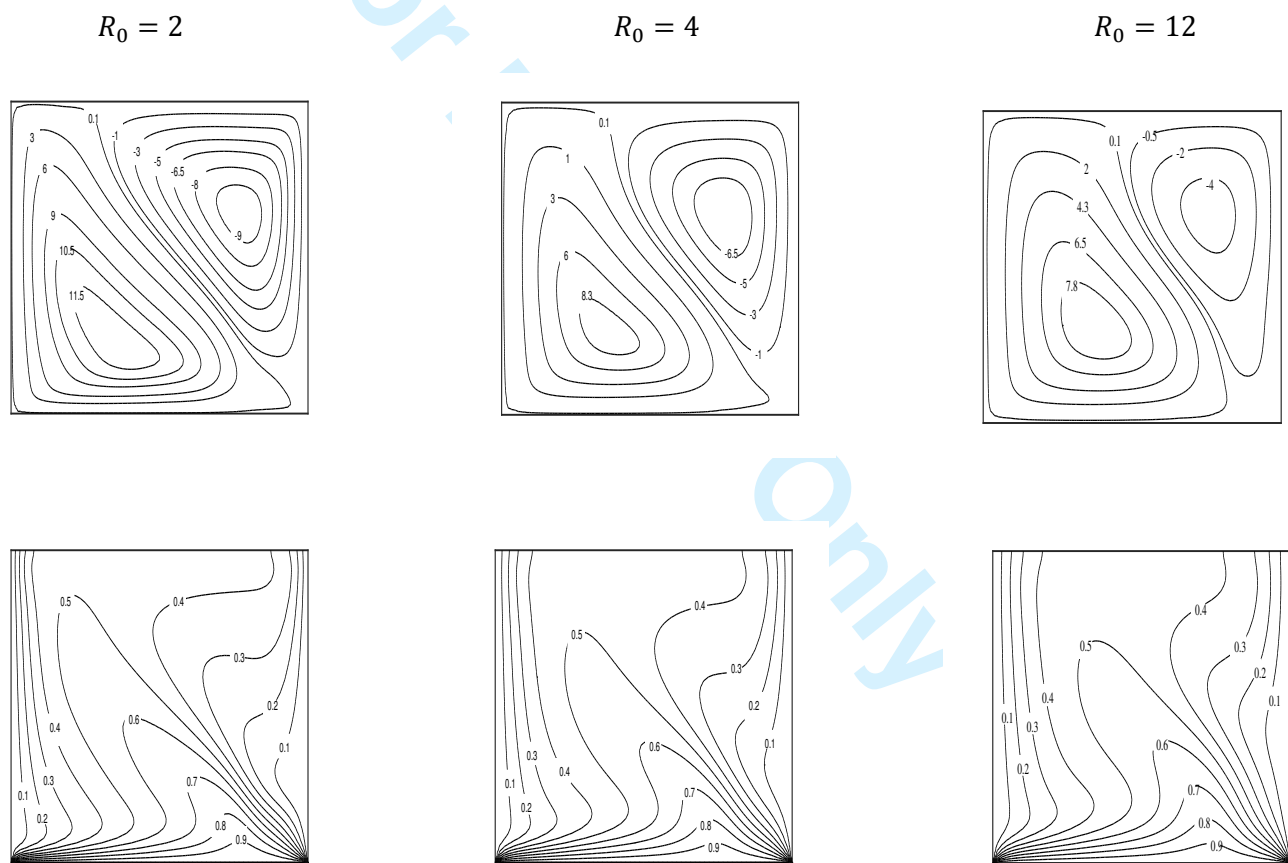
$R_0 = 2$ $R_0 = 4$ $R_0 = 12$

Fig. 7: Effects of micropolar parameter on streamlines and isotherms for $Gr = 10^6, Da = 10^{-3}, Ha = 10, \phi = \omega = 45^0$

26

$$\phi = 0^0 \qquad\qquad \phi = 45^0 \qquad\qquad \phi = 90^0$$

$\omega = -45^0$

$\omega = 0^0$

$\omega = 45^0$

Fig. 8: Effects of ϕ and ω on streamlines for $Gr = 10^6, R_0 = 2, Da = 10^{-3}, Ha = 50, Pr = 1$

$\phi = 0^0$ $\phi = 45^0$ $\phi = 90^0$

$\omega = -45^0$

$\omega = 0^0$

$\omega = 45^0$

Fig. 9: Effects of ϕ and ω on isotherms for $Gr = 10^6, R_0 = 2, Da = 10^{-3}, Ha = 50, Pr = 1$
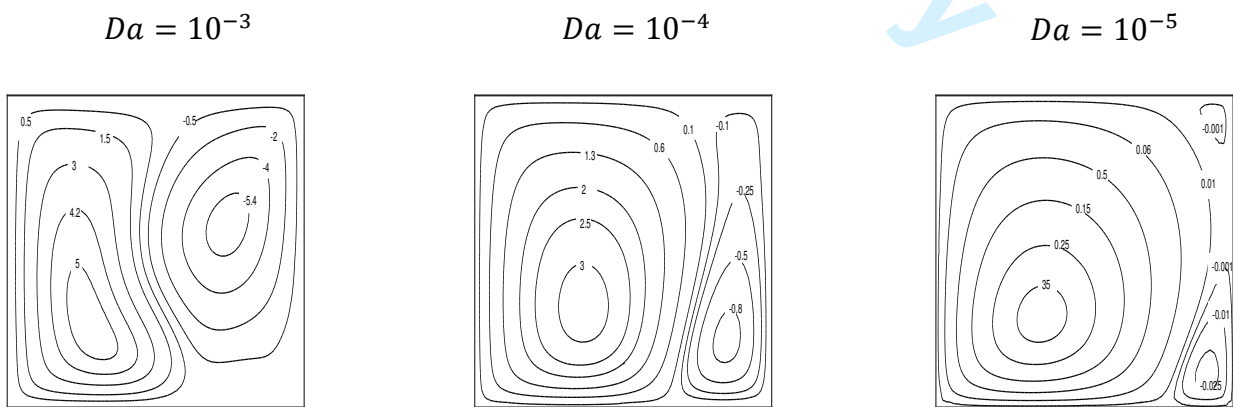
28

$Pr = 0.015$　　　　$Pr = 7$　　　　$Pr = 1000$　　　　$Pr = 10000$

Fig. 10: Effects of Prandtl number on streamlines and isotherms for $Gr = 10^6, R_0 = 2, Ha = 150, \phi = \omega = 45^0,$
$Da = 10^{-3}$

$Da = 10^{-3}$　　　　$Da = 10^{-4}$　　　　$Da = 10^{-5}$

29

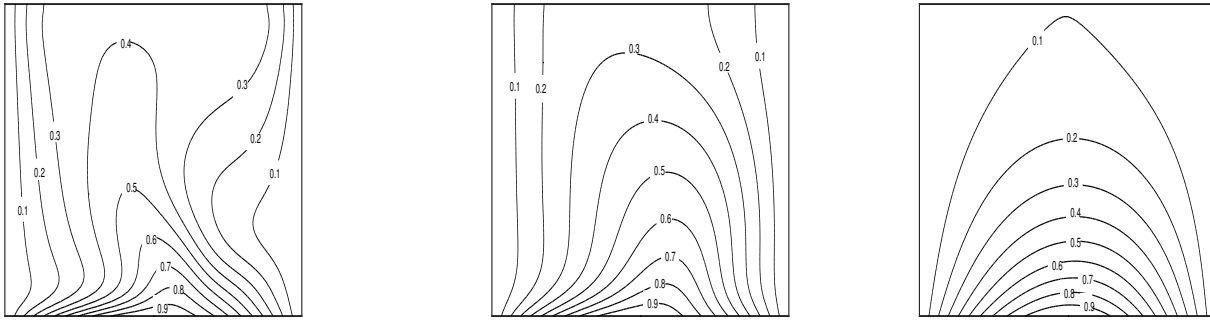Fig. 11: Effects of Darcy number on streamlines and isotherms for $Gr = 10^6, R_0 = 2, Ha = 60, \phi = \omega = 45^0$
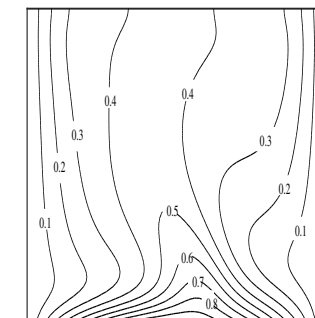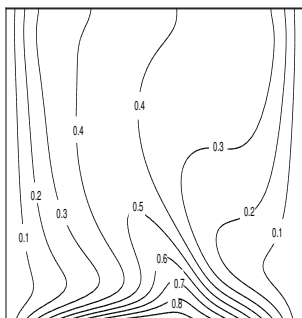
$R_0 = 0$ $R_0 = 4$ $R_0 = 12$
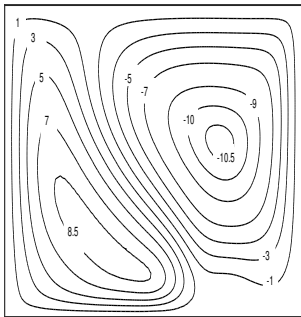
12: Effects of micropolar parameter on streamlines and isotherms for $Gr = 10^6, Da = 10^{-3}, Ha = 10, \phi = \omega = 45^0$
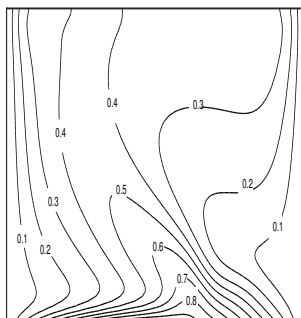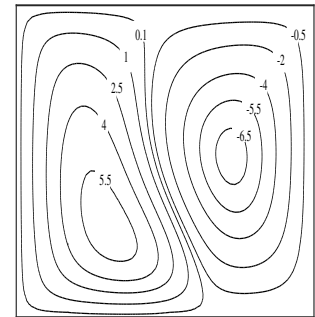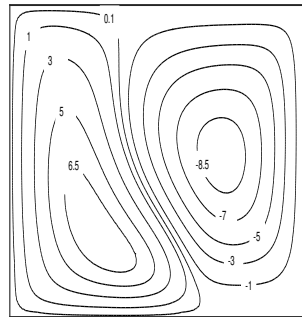
$R_0 = 12$ $R_0 = 12$
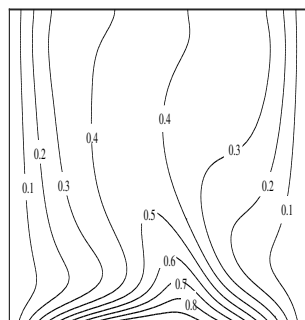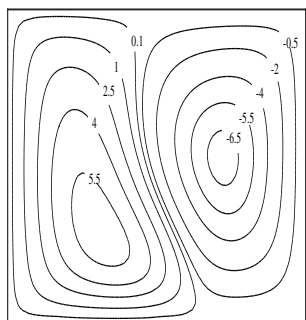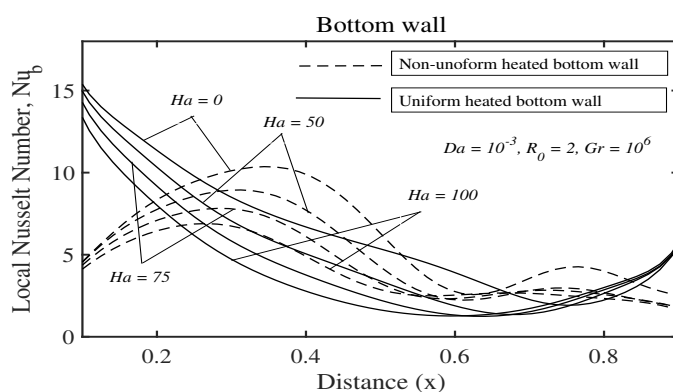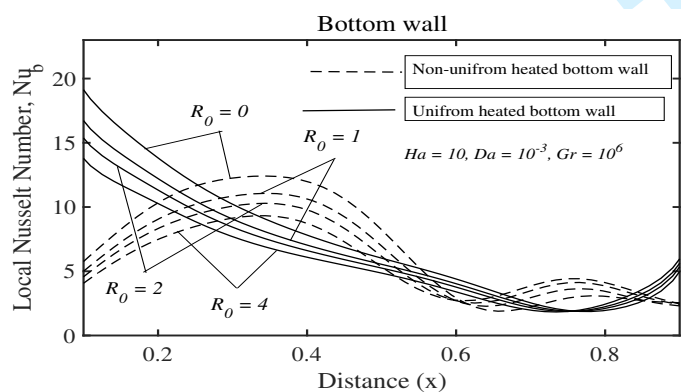
Fig. 13: Effects of micropolar parameter on streamlines and isotherms for weak concentration $Gr = 10^6, \phi = \omega = 45^0,$
$Da = 10^{-3}, Ha = 10$.

(a)   (b)

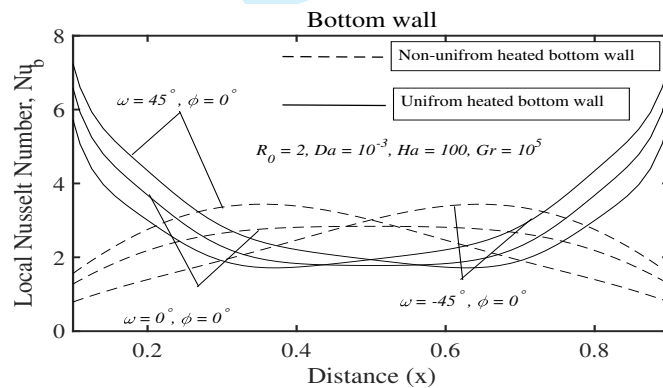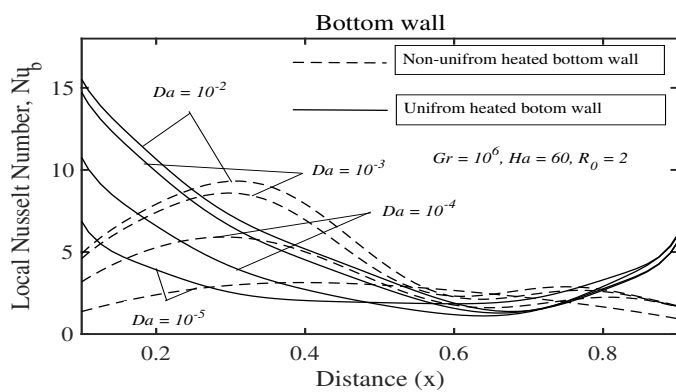(c)   (d)

Fig.14: variation of local Nusselt number against (a) micropooar parameter, (b) Hartman number, (c) Darcy number and (d) inclination angle.

Table 2

χ	ω	Gr	[41] $\overline{Nu_h}/\chi$ $(Ha=0)$	Present work $\overline{Nu_h}/\chi$ $(Ha=0)$	[41] $\overline{Nu_h}/\chi$ $(Ha=100)$			Present work $\overline{Nu_h}/\chi$ $(Ha=100)$		
					$\phi=0^0$	$\phi=45^0$	$\phi=90^0$	$\phi=0^0$	$\phi=45^0$	$\phi=90^0$
1	0^0	10^3	3.7458	3.7603	3.6814	3.6770	3.6787	3.7054	3.6875	3.6891
--	----	10^4	4.7716	4.7767	3.6831	3.6819	3.6813	3.6842	3.6823	3.6816
--	----	10^5	6.6773	6.6780	3.8242	3.9447	3.8852	3.8249	3.9450	3.8855
--	-45^0	10^3	3.7555	3.7544	3.6829	3.6801	3.6802	3.6824	3.6798	3.6796
--	----	10^4	4.5528	4.5510	3.6806	3.6846	3.6843	3.6800	3.6840	3.6846
--	----	10^5	6.3797	6.3740	3.8546	3.8774	3.8750	3.8539	3.8757	3.8730
--	45^0	10^3	3.6828	3.6812	3.6803	3.6815	3.6801	3.6798	3.6809	3.6791
--	----	10^4	4.3342	4.3321	3.6780	3.6820	3.6801	3.6776	3.6802	3.6755
--	----	10^5	5.6870	5.6730	3.7032	3.6833	3.7119	3.6935	3.6736	3.7028

Table 3

Variation of the average Nusselt number at hot wall of the conduit

Pr	ω	Gr	Da	Ha	ξ	R_0	η	Uniform Heated			Non-uniform/Sinusoidal heated		
								$\phi=0^0$	$\phi=45^0$	$\phi=90^0$	$\phi=0^0$	$\phi=45^0$	$\phi=90^0$
1	0^0	10^3	10^{-3}	100	0.5	2	1	6.1472	6.1472	6.1472	1.9925	1.9926	1.9927
---	----	10^4	----	----	---	---	---	6.1477	6.1479	6.1482	1.9998	2.0005	2.0022
---	----	10^5	----	----	---	---	---	6.1702	6.1958	6.2479	2.0919	2.1177	2.1714
---	-45^0	10^3	----	----	---	---	---	6.1472	6.1472	6.1472	1.9923	1.9921	1.9924
---	----	10^4	----	----	---	---	---	6.1478	6.1476	6.1480	1.9977	1.9955	1.9992

							$R_0=0$	$R_0=2$	$R_0=4$	$R_0=0$	$R_0=2$	$R_0=4$
---	----	10^5	----	----	---	---	6.2004	6.1916	6.2071	2.0850	2.0602	2.1098
---	45^0	10^3	----	----	---	---	6.1472	6.1472	6.1472	1.9923	1.9926	1.9924
---	----	10^4	----	----	---	---	6.1484	6.1484	6.1481	1.9977	2.0008	1.9992
---	----	10^5	----	----	---	---	6.2021	6.2232	6.2084	2.0854	2.1300	2.1101

Table 4

Variation of the average Nusselt number at hot wall of the conduit with $\phi = 45^0, \chi = 1$.

η	ω	Da	Gr	Ha	ξ	Pr	Uniform Heated			Non-uniform/Sinusoidal heated		
							$R_0=0$	$R_0=2$	$R_0=4$	$R_0=0$	$R_0=2$	$R_0=4$
1	0^0	10^{-2}	10^5	100	0.5	1	6.2724	6.2326	6.2131	2.2183	2.1625	2.1330
---	----	10^{-3}	----	----	---	---	6.2118	6.1958	6.1871	2.1495	2.1177	2.0997
---	----	10^{-4}	----	----	---	---	6.1560	6.1544	6.1535	2.0403	2.0344	2.0307
---	-45^0	10^{-2}	----	----	---	---	6.2233	6.2135	6.2066	2.0929	2.0752	2.0650
---	----	10^{-3}	----	----	---	---	6.1969	6.1916	6.1969	2.0734	2.0602	2.0525
---	----	10^{-4}	----	----	---	---	6.1554	6.1546	6.1542	2.0231	2.0195	2.0173
---	45^0	10^{-2}	----	----	---	---	6.3342	6.2819	6.2563	2.2655	2.1983	2.1626
---	----	10^{-3}	----	----	---	---	6.2422	6.2232	6.2126	2.1665	2.1300	2.1127
---	----	10^{-4}	----	----	---	---	6.1590	6.1573	6.1564	2.0336	2.0287	2.0256

10^{-3}	0	0	---	6.9542	6.7587	6.6550	2.9234	2.6358	2.5018
--	50	---	---	6.5282	6.4393	6.3903	2.4833	2.3518	2.2842
--	100	---	---	6.2422	6.2231	6.2123	2.1665	2.1320	2.1123
10^{-3}	100	---	0.015	6.2721	6.2440	6.2276	2.1869	2.1477	2.1247
--	100	---	7	6.2415	6.2229	6.2125	2.1661	2.1321	2.1129
--	100	---	1000	6.2011	6.1837	6.1739	2.1455	2.1148	2.0977

References

1. A. Bejan, and C.L. Tien. ASME J. Heat Transfer, **100**, 641 (1978).

2. G. D. V. Davis. Int. J. for Numer. Methods in Fluids, **3**, 249 (1983).

3. K. L. Gou and S. T. Wu. J Sol Energy Eng., **107**, 15 (1985).

4. J. D. Hall, A. Bejan and J. B. Chaddock. Int. J. Heat and Fluid Flow, **9**, 396 (1988).

5. J. C. Patterson and S. W. Armfield. J. Fluid Mechanics, 219, 469 (1990).

6. R. A. Kuyper, T. H. V. D. Meer, C. J. Hoogendoorn and R. A. W. M. Henkes. Int. J. Heat Mass Transfer, **36**, 2899 (1993).

7. M. R. Ravi, R. A. W. M. Henkes and C. J. Hoogendoorn. J. Fluid Mechanics, **262**, 325 (1994).

8. G. Barakos, E. Mitsoulis and D. Assimacopoulos. Int. J. Numer. Methods Fluids, **18**, 695 (1994).

9. H. Ozoe and M. Maruo. JSME Int. J., **30**, 774 (1987).

10. H. Ozoe and K. Okada. Int. J. Heat Mass Transfer, **32**, 1939 (1989).

11. P. Vasseur, M. Hasnaoui, E. Bilgen, and L. Robillard. ASME J. Heat Transfer, **117**, 121 (1995).

12. D.G. Cormack, L.G. Leal and J. Imberger. J. Fluid Mechanics, **65**, 209 (1974).

13. S. Alchaar, P. Vasseur, E. Bilgen, J. Heat Trans. **117**, 668 (1995).

14. J. P. Garandet, T. Alboussiere, and R. Moreau. Int. J. Heat Mass Transfer, **35**, 741 (1992).

15 N. Rudraiah, R. M. Barron, M. Venkatachalappa, and C. K. Subbaraya. Int. J. Eng. Sci., **33**, 1075 (1995).

16. G. M. Oreper and J. Szekely. J. Crys. Groth, **64**, 505 (1983).

17 S. Alchaar, P. Vasseur and E. Bilgen. Chem. Eng. Comm., **134**, 195 (1995)

18. K. Vafai. CRC Press, USA. **2**, 1 (2005).

19. K. Vafai. CRC Press, USA. **1**, 1 (2011).

20. C. K. Chen and C. R. Lin. Int. J. Eng. Sci., **33**, 131 (1995).

21. T. W. Tong and E. Subramanian. Int. J. Heat Mass Transfer, **28**, 563 (1985).

22. G. Lauriat and V. Prasad. ASME, J. Heat Transfer, **109**, 295 (1987).

23. T. Basak, S. Roy, T. Paul, and I. Pop. Int. J. Heat Mass Transfer, **49**, 1430 (2006).

24. K. L. Walker and G. M. Homsy. J. Fluid Mech., **87**, 449 (1978).

25. V. Prasad and F. A. Kulacki. ASME, J. Heat Transfer, **106**, 158 (1984).

26. Basak, T., Roy, S., Singh, S. K., Pop, I., Int. J. Heat Mass Transfer **52**, 4135 (2009).

27. A.C. Eringen. Springer, New York, **I**, 1 (2001).

28 G. Łukaszewicz. Birkhäuser, Basel, 1 (1999).

29 A.C. Eringen. Int. J. Eng. Sci. **2**, 205 (1964).

30 A. C. Eringen. J. Math. Mech. **16**, 1 (1966).

31. A. C. Eringen. J. Math. Anal. Appl. **38**, 480 (1972).

32. T. Hayat, M. I. Khan, M. Waqas and A. Alsaedi. Results in Physics **7**, 446 (2017).

33. T. Hayat, M. I. Khan, M. Farooq, T. Yasmeen and A. Alsaedi, J. Mol. Liq., **220**, 49 (2016).

34. T. Hayat, M. I. Khan, M. Farooq, A. Alsaedi, M. Waqas and T. Yasmeen. Int. J. Heat Mass Transfer, **99**, 702 (2016).

35. M. Farooq, M. I. Khan, M. Waqas, T. Hayat, A. Alsaedi and M. I. Khan. J. Mol. Liq. **221**, 1097 (2016).

36. M. I. Khan, T. Hayat, M. I. Khan and A. Alsaedi. Int. J. Heat Mass Transfer, **113**, 310 (2017).

37. M. I. Khan, M. Waqas, T. Hayat, M. I. Khan and A. Alsaedi. Int. J. Mech. Sci., **131–132**, 426 (2017).

38. M. I. Khan, M. Waqas, T. Hayat, A. Alsaed. J. Colloid Interface Sci., **498**, 85 (2017).

39. M. I. Khan, M. I. Khan, M. Waqas, T. Hayat, A. Alsaedi, Int. Com. Heat Mass Transfer, **86**, 231 (2017).

40. T. Hayat, M. I. Khan, M. Waqas, A. Alsaedi, and M. I. Khan. Int. Com. Heat Mass Transfer **86**, 231 (2017).

41. M. Waqas, M. Farooq, M. I. Khan, A. Alsaedi, T. Hayat and T. Yasmeen. Int. J. Heat Mass Transfer, **102**, 766 (2016).

42. Z. Iqbal, R. Mehmood, E. Azhar and Z. Mehmood. Eur. Phys. J. Plus, **132**, 175 (2017).

43. S. Nadeem, S. Masood, R. Mehmood and M. A. Sadiq. PLoS ONE, **10**, 1 (2015).

44. S. Nadeem, R. Mehmood and S. Masood. J. Magn. Magn. Mater. **401**, 1006 (2016).

45. R. Tabassum, R. Mehmood and S. Nadeem. J. Colloid Interface Sci. **501**, 304 (2017).

46. S. K. Jena and S.P. Bhattacharyya. Int. J. Sci. Engng., **24**, 69 (1986).

47. T. H. Hsu and C. K. Chen. Int. J. Engng Sci., **34**, 407 (1996).

48. S.G. Wang and T. H. Hsu, Mathl. Comput. Modelling, **17**, 73 (1993).

49. G. C. Bourantas and V. C. Loukopoulos. Int. J. Heat Mass Transfer, **79**, 930 (2009).

50. N. S. Gibanov, M. A. Sheremet and I. Pop. Int. J. Heat Mass Transfer. **99**, 831 (2016).

51. M. Zadravec, M. Hribersek and L. Skerget. Eng. Anal. Boundary Elem., **33**, 485 (2009).

52. N. S. Gibanov, M. A. Sheremet and I. Pop. J. Mol. Liq., **221**, 518 (2016).

53. M. A. Sheremet, I. Pop and A. Ishak. Int. J. Heat Mass Transfer. **105**, 610 (2017).

54. Z. Alloui and P. Vasseur. Int. J. Heat Mass Transfer. **53**, 2750 (2010).

55. M. C. Ece, E. Buyuk. Fluid Dyn. Res. **38**, 564 (2006).

56. M. A. Sheremet, I. Pop and O. Mahian. Int. J. Heat Mass Transfer **116**, 751 (2018).

57. J. A. Shercliff. Pergamon Press, Oxford, 1 1965.

58. H. T Cheong, Z. Siri and S. Sivasankaran. Int. Commun Heat Mass Transfer; **45**, 75 (2013).

59. N. H. Saeid and Y. Yaacob. Numer Heat Transfer A, **49**, 683 (2006).

60. E. Natarajan, T. Basak and S. Roy, Int. J Heat Mass Transfer, **51**, 747(2008).

61. I. E. Sarris, I. Lekakis and N. S. Vlachos. Numer. Heat Transf. A, **42**, 513 (2002).

62. I. E. Sarris, N. Katsavos, I. Lekakis and N.S. Vlachos, Proceedings of the 6th National Conference of Solar Technology Institute, Greece, **2**, 201 (1999).

63. Bouhalleb and Abbassi, Int. J. Hydrog. Energy, 13676 (2015).

64. W. J. Minkowycz, E. M. Sparrow, G. E. Schneider and R. H. Fletcher. Numerical Heat Transfer, Wiley, New York. 1 (1988).

65. J. N. Reddy, McGraw Hill, New York, pp. 01 (1993).

66. T. Basak, S. Roy and A. R. Balakrishnan. Int. J. Heat Mass Transfer, **49**, 4525 (2006).